Solar Energy 263 (2023) 111935

Contents lists available at ScienceDirect

Solar Energy

journal homepage: www.elsevier.com/locate/solener

Techno-economic assessment of a numbering-up approach for a 100 MW_e third generation sodium-salt CSP system

Charles-Alexis Asselineau [a,b,1], Armando Fontalvo [a,1], Shuang Wang [a], Felix Venn [a], John Pye [a], Joe Coventry [a,*]

[a] School of Engineering, The Australian National University, Acton, 2601, ACT, Australia
[b] IMDEA Energy, Av. Ramón de La Sagra, 3, Móstoles, 28935, Madrid, Spain

ARTICLE INFO

Keywords:
Concentrated solar power
Central receiver systems
Liquid sodium
Chloride salt
Numbering-up
Techno-economic analysis

ABSTRACT

This work presents the design and techno-economic analysis of a 100 MW_e concentrated solar power (CSP) system using a supercritical CO_2 power block with 700 °C input temperature. Aiming to leverage the relatively higher efficiency of small heliostat fields and potential multi-build discounts, a numbering-up approach is examined, developing four alternative configurations (1×100, 2×50, 3×33, and 4×25 MW_e), in which each module has its own dedicated tower, heliostat field, receiver, thermal storage and power block. A comprehensive techno-economic model is combined with detailed annual simulations to yield levelised cost of energy (LCOE) estimations and analyse the potential of system numbering-up for high-temperature next-generation CSP systems based on liquid heat transfer fluids (HTFs). The simulations are verified against the System Advisor Model with differences in the LCOE calculations within ±1.0%. Comparing the four systems shows that a 1×100 MW_e system leads to an LCOE of 54.88 USD/MWh_e, lower than for the numbered-up modules. However, the LCOE difference between configurations with one and two modules is moderate, with the 2×50 MW_e configuration showing an LCOE of 55.99 USD/MWh_e (+2%). Despite their higher annual conversion efficiencies, the 3×33 MW_e and 4×25 MW_e systems are more capital-intensive and escalate LCOE by 6.9 and 12.2%, respectively. With size-dependent power block efficiency, further LCOE escalation with numbered-up systems is observed, however, multi-build savings could potentially reverse this cost escalation and a 13.9–19.6% saving on the two-module system would allow them to break even.

1. Introduction

Commercial concentrated solar power (CSP) tower technologies employ molten nitrate salt as the heat transfer fluid (HTF) and a steam-based Rankine cycle power block. The gross thermal-to-electricity efficiency of the cycles in commercial central receiver systems (CRSs) is typically between 30%–40% at inlet temperatures <600 °C. At higher inlet temperatures, efficiency can increase following Carnot's theorem and this has motivated recent efforts in the development of supercritical CO_2 (sCO_2) Brayton cycles [1].

At temperatures higher than 600 °C, molten salt becomes chemically unstable and corrosive [2]. Liquid sodium has been studied as a possible heat transfer fluid for central receiver systems [3] including in systems operating at temperatures above 700 °C [4–6]. Liquid sodium has a very high thermal conductivity, which reduces thermal gradients and associated thermal stresses in the receiver pipe walls during operations, thus enabling high concentrated fluxes [7], and ultimately greater heat-transfer efficiencies.

While economies of scale tend to favour large systems over multiple smaller ones, the determination of the optimal size of the components of a CSP system is a complex problem as many interacting factors lead to non-obvious trade-offs. The solar sub-system (tower, receiver and heliostat field) represents more than half the capital cost of a plant and is complex to size properly because:

- The heliostat field layout is strongly dependent on both the tower height and system capacity, in addition to system location and atmospheric conditions.
- The receiver design and efficiency depend on the field layout.
- The tower design (including internal parts) is a function of the receiver weight and does not vary linearly with height.

* Corresponding author.
E-mail addresses: charles-alexis.asseslineau@anu.edu.au (C.-A. Asselineau), armando.fontalvo@anu.edu.au (A. Fontalvo), shuang.wang@anu.edu.au (S. Wang), felix@renewengineering.com.au (F. Venn), john.pye@anu.edu.au (J. Pye), joe.coventry@anu.edu.au (J. Coventry).
[1] These authors contributed equally and share co-first authorship.

https://doi.org/10.1016/j.solener.2023.111935
Received 20 April 2023; Received in revised form 10 July 2023; Accepted 3 August 2023
Available online 17 August 2023

Nomenclature

Abbreviations

DNI	Direct normal irradiance (W/m^2)
HTF	Heat transfer fluid
HTR	High-temperature recuperator
LCOE	Levelised cost of energy (USD/MWh_e)
LTR	Low-temperature recuperator
PB	Power block
PHX	Power block primary heat exchanger
SAM	System Advisor Model
SM	Solar multiple
TES	Thermal energy storage

Symbols

A	Area (m^2)
C	Cost (USD)
D	Diameter (m)
d	Tube diameter (m)
E	Energy (J)
G	Direct normal irradiance (W/m^2)
g	Gravitational acceleration (m/s^2)
H	Height (m)
h	Enthalpy (kJ/kg)
h_{conv}	Convective heat transfer coefficient (W/m^2 K)
L	Length (m)
l_p	Panel width (m)
$\dot{m}$	Mass flow rate (kg/s)
m	Mass (kg)
N_{fp}	Number of flow paths
N_p	Number of panels
N_{sys}	Number of systems
N_t	Number of pipes per panel
$\dot{Q}$	Heat transfer rate (W_{th})
R_c	Field minimum radius
T	Temperature (K)
U	Overall heat transfer coefficient (W/m^2 K)
v	Velocity (m/s)
$\dot{W}$	Power (W_e)

Greek symbols

α	Solar elevation angle (°)
α_{eff}	Effective coating absorptivity (–)
ΔP	Pressure drop (Pa)
δ	Solar declination angle (°)
δ_t	Tube spacing (m)
ϵ_{eff}	Effective coating emissivity (–)
η	Energy conversion efficiency
η_q	PHX off-design thermal fraction
ω	Solar hour angle (°)
ρ	Density (kg/m^3)
σ	Stefan–Boltzmann constant (5.67×10^{-8} W/m^2 K)

Subscripts

amb	Ambient
aux	Auxiliary heat supply
av	Availability
base	Power output independent
boc	Balance of costs
conv	Convection
cool	Power block cooling system
des	Design-point condition
emi	Emission
field	Heliostat field
fp	Flow path
gross	Gross thermal or power output
hel	Heliostats
hx	Heat exchanger
i	Inner
in	Inlet
loss	Heat or power loss
mat	Material
Na	Liquid sodium stream
net	Net thermal or power output
o	Outer
opt	Optical
out	Outlet
par	Parasitic loss
pipe	Riser or downcomer pipe
piping	Riser, downcomer, or cold salt piping
pump	Sodium or salt pump
rec	Receiver
ref	Reference
salt	Chloride salt stream
th	Thermal
variable	Power output dependent
w	External wall

The efficiency of the solar subsystem of a CRS notably depends on the system capacity. As the power block design output and storage design capacity increase, the heliostat field and receiver dimensions increase. The larger the heliostat field, the larger the optical losses, particularly so for cosine, attenuation and spillage losses [8]. Smaller CRSs show higher solar subsystem efficiency, mostly thanks to better heliostat field optics, and this has motivated research into modular CSP configurations where large solar subsystems are split into smaller ones with higher efficiency. Some studies have specifically focused on the optics of modular CSP [9–11], with a focus on the improvement of annual optical efficiency through efficient field-tower layouts, and intelligent allocation of heliostats to specific receivers. While research in this field is ongoing, optimal modular CSP configurations must maximise the revenue generated, which is dependent on both system efficiency and cost as presented in [12–14]. Beyond research, a few companies have developed [15] and tested prototype modular CSP systems [16].

All the above-mentioned studies assume the use of steam Rankine power blocks, which suffer significant cost and efficiency penalties at small scales. As a consequence, modular CSP configurations have focused on the use of a single central power block which imposes the use of HTF transport networks that take the HTF from the power block to the receivers and back. HTF transport networks add cost and energy losses to the system. sCO_2 turbomachinery is significantly more compact than for steam Rankine cycles and remains efficient at lower

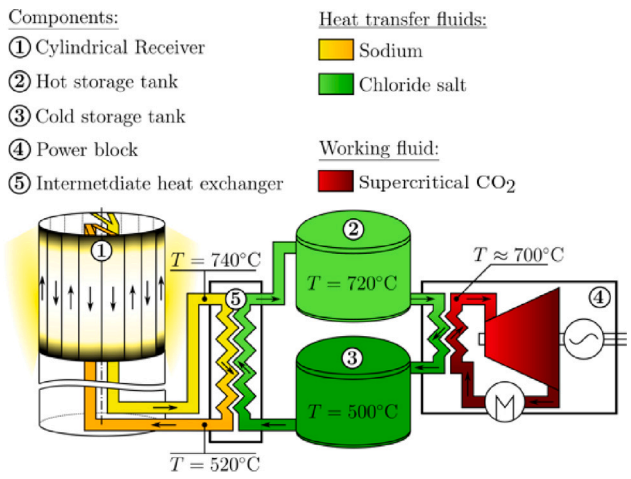

Fig. 1. Schematic of the third generation sodium-salt CSP system evaluated in this study.

capacities [17], thus opening the possibility of using a "numbering-up" modular approach where large systems are completely split into smaller systems, each with their own power block.

This work evaluates a numbering-up approach for a 100 MW_e CSP system using a sCO_2 power block with 700 °C input temperature. The system is designed with 4 alternative configurations, from one to four independent systems. A comprehensive techno-economic model is used, in combination with detailed annual simulations, to yield LCOE estimations and analyse the potential of system numbering-up for high-temperature next-generation CSP systems based on Liquid HTFs. It is imperative to note that the calculated LCOE is in reference to the long-term design considerations and advanced technologies for CSP plants, which is substantially different from present-day nitrate salt CSP plants. As this study suggests, future advancements in CSP technology, such as those envisioned by the U.S. Department of Energy's Gen3 CSP programme [18,19], may result in significantly lower LCOEs.

2. Methods

2.1. System configuration

The system of consideration is an indirect CRS in which the receiver and two tank storage systems use different HTFs. In the receiver, liquid sodium is heated from 520 °C to 740 °C. Liquid sodium exchanges heat with a ternary $MgCl_2$-KCl-NaCl salt [1,20] in a shell and tube heat-exchanger at the bottom of the tower and the chloride salt acts as the storage medium in a two-tank molten salt storage system operating between 500 °C and 720 °C. The power block primary heat exchanger transfers heat from the hot chloride salt to sCO_2, such that the inlet temperature to the turbine is 700 °C. The system configuration is summarised in Fig. 1.

2.2. Solar subsystem design

2.2.1. Simplified design methodology

Splitting a 100 MW_e output into $N_{sys} = 1$, 2, 3 or 4 identical systems leads to CRSs with power block capacities ($\dot{W}_{net,des}$) of 100 MW_e, 50 MW_e, 33 MW_e, and 25 MW_e. Co-optimisation of the field and receiver designs is necessary to obtain an optimal solar sub-system. However, this task is computationally expensive, difficult to fully automatise and therefore challenging to include in a broad parametric study. Instead, a simplified field/receiver design method is chosen to make this study tractable, with the caveat that the resulting solar subsystem designs may not be exactly at their optimal configuration. In the first step, the receiver thermal design capacity is approximated assuming a power block efficiency of $\eta_{PB,des}$ = 51%, 1% of parasitic power loss ($\eta_{par,des}$ = 99%), a receiver design point absorbed-thermal efficiency of $\eta_{rec,th,des}$ = 85% and a solar multiple of SM = 3. The resulting receiver design thermal input capacities $\dot{Q}_{rec,des}$ are 175 MW_{th}, 230 MW_{th}, 350 MW_{th} and 700 MW_{th} (Eq. (1)).

$$\dot{Q}_{rec,des} = SM \frac{100 \times 10^6}{N_{sys}\eta_{PB,des}\eta_{par,des}\eta_{rec,th,des}} \quad [MW_{th}] \tag{1}$$

The design of the field and receiver for each of these design thermal capacities then proceeds in two steps:

- First, the heliostat field and receiver diameter are determined based on maximised annual intercepted power estimation using a fast convolution optics method (cf. 2.2.2).
- Following this step, the receiver height and aiming strategy are established, based on design point conditions and using more detailed modelling (cf. 2.2.3).

Table 1
SolarPILOT annual simulation parameters for the field layout and receiver diameter determination.

Day number	Month	Day	DNI (W/m²)	Daily DNI (kWh/m²)	Time points
11	Jan.	11	650.5	2.5	6
57	Feb.	26	664.6	3.0	7
103	Apr.	13	774.4	3.8	8
148	May	28	820.0	4.5	9
194	Jul.	13	833.6	4.7	9
240	Aug.	28	870.9	4.4	8
285	Oct.	12	847.0	3.9	7
330	Nov.	27	739.7	3.0	6
					60

Table 2
Power block design capacities $\dot{W}_{net,des}$, receiver design thermal power $\dot{Q}_{rec,des}$, tower heights H_{tower}, field minimum radius R_c and receiver diameter D_{rec} evaluated in the field and receiver diameter determination step of the design.

$\dot{W}_{PHX,des}$	$\dot{Q}_{rec,des}$	H_{tower}	R_c	D_{rec}
25 MW_e	175 MW_{th}	100 m to 200 m	50 m	5 to 15 m
33 MW_e	230 MW_{th}		57 m	6 to 16 m
50 MW_e	350 MW_{th}		70.5 m	7 to 17 m
100 MW_e	700 MW_{th}		92 m	10 to 20 m

2.2.2. Heliostat field and receiver diameter determination

The SolarPILOT software from NREL [21] is used to optimise heliostat field designs based on maximised annual thermal input to the receiver for a range of receiver diameters and tower heights. The annual simulation is based on the 60 time points shown in Table 1. The location of the plant is Daggett (CA, USA) and TMY2 Direct Normal Irradiance (DNI) data is used.

The minimum radius of the field (R_c) – i.e. the distance from the tower centre to the nearest heliostat– was adjusted for configurations with different power capacity in order to reflect the different sizes of the power block, storage and balance of plant installations at the bottom of the tower. Similarly, the receiver diameters (D_{rec}) evaluated for each plant capacity are adapted in order to minimise the number of simulations of sub-optimal designs. The maximum field radius is set at 2 km for all capacities. Finally, 5 tower heights (H_T) are considered: 100 m, 125 m, 150 m, 175 m and 200 m. The heliostats simulated (Table 3) have similar reflective area and optical error to the Stellio heliostat by Schlaich Bergermann Partner, used in the recent Hami power plant [22]. The field design parameters are summarised in Table 2.

Optimal heliostat field layouts are typically much less sensitive to receiver height than to receiver diameter. This is because the receiver height is generally designed large enough such that the heliostat field aiming strategy can distribute the flux on the receiver surface and

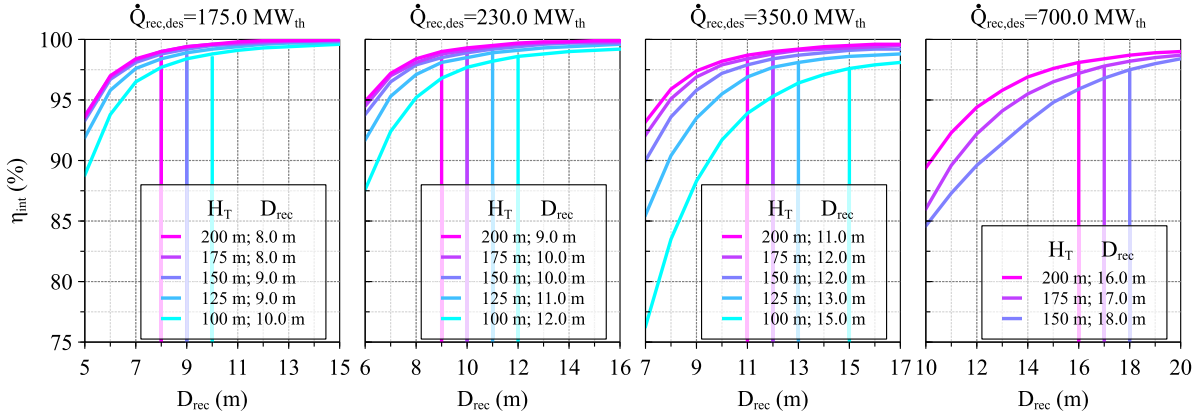

Fig. 2. Receiver design diameter selection for each tower height and receiver design capacity based on the value of the achievable intercept factor. The receiver diameter values in the legend are the selected configurations. (For interpretation of the references to colour in this figure legend, the reader is referred to the web version of this article.)

Table 3
Heliostat modelling assumptions.

Parameter	Value
Dimensions	7.07 m by 7.07 m
Surface area	50 m^2
Reflectance	90%
Slope error	1.5 mrad
Facet design	Single facet
Focal length	Slant range

reduce the risk of thermo-mechanical failure of the receiver tubes. At this stage of the design, the receiver height is overestimated to 35 m to ignore the effect of the spillage of radiation at the top and bottom of the receiver on the optical efficiency and focus on the selection of an appropriate diameter. The aiming strategy is set to the "simple aim points" option in SolarPILOT, which is the equatorial aiming (i.e. aiming at the receiver mid-height).

In total, 10 receiver diameters, 4 values of receiver design thermal input and 5 different tower heights are simulated, leading to 200 configurations. The configurations with tower heights below 150 m for the larger systems (700 MW_{th}) cannot meet the design thermal capacity at the design point and are therefore ignored in the rest of this study.

For each combined tower height and thermal design capacity evaluated, the selected configuration is the one that has an intercept factor superior to 99% of the maximum intercept factor achieved by all configurations at equinox solar noon with the smallest receiver diameter. Fig. 2 illustrates the selection of the 18 systems taken to the second stage of the design.

2.2.3. Receiver height determination

In the second step of the design process, the 18 selected systems are modelled with a comprehensive multi-physics heat-transfer model that includes 3D ray-tracing simulation for the optical concentration process coupled with an energy, mass and momentum balance model based on a 1D finite differences formulation for each tube bank. The specific ray-tracing software used is Solstice from CNRS PROMES, scripted thanks to a modified version of the Python-based API developed at the ANU [23]. The energy model uses the Python-based model presented in [24]. For each configuration, the receiver height is varied in a range starting from the receiver diameter to this value plus 10 m, with 1 m height increments. For reasons including corrosion/erosion rates and flow-induced vibrations, maximum flow velocity limits for liquid sodium in tubes have been devised in the past for the nuclear industry [25]. For tube diameters below 101.6 mm, the recommended maximum velocity of 2.44 m/s is adopted in this study. In addition to this value, a minimum evaluated flow velocity of 1 m/s is established to avoid generating designs with slow flows that would penalise the heat transfer coefficient and ultimately result in lower thermal efficiency.

In order to avoid the simulation of a large number of unfeasible configurations with the detailed model, the number of tube panels and the flow-path configurations are pre-established with a dedicated heuristic. The density of liquid sodium is the lowest at the outlet temperature of the receiver flow paths and, therefore, an upper bound of velocity can be determined using the density at the receiver outlet in Eq. (2).

$$v_{HTF,des} \approx \frac{\dot{m}_{HTF,des}}{N_t \cdot \rho_{HTF,out,des} \cdot \frac{\pi d_{t,i}^2}{4}} \tag{2}$$

The mass flow is determined by the division of the net heat gain per flow path ($\dot{Q}_{fp,net,des}$) by the specific enthalpy gain in the receiver (Eq. (3)).

$$\dot{m}_{HTF,des} = \frac{\dot{Q}_{fp,net,des}}{h_{HTF,out,des} - h_{HTF,in,des}} \tag{3}$$

As the energy balance is not solved at this stage, the net heat gain per flow path (Eq. (4)) is unknown and two assumptions are made to approximate it. First, $\dot{Q}_{fp,net}$ is conservatively approximated as equal to the incident flux in each flow path, which results in overestimated heat gains and hence in overestimated velocities. Second, without a-priori knowledge of the flux distribution between the banks of the receiver, the net flux gain per flow path is assumed identical for all flow paths.

$$\dot{Q}_{fp,net,des} \approx \frac{\dot{Q}_{rec,inc,des}}{N_{fp}} \tag{4}$$

For a given receiver diameter D_{rec} and number of panels N_p, the width of the panels l_p can be determined with Eq. (5).

$$l_p = D_{rec} \cdot \sin\left(\frac{\pi}{N_p}\right) \tag{5}$$

The number of tubes per panel is obtained by division of the panel width by the tube outer diameter (including tube spacing δ_t, assumed as 1 mm in this work), rounded down (Eq. (6)).

$$N_t = \left\lfloor \frac{l_p}{d_{t,out} + \delta_t} \right\rfloor \tag{6}$$

For each receiver diameter and thermal capacity, bank numbers between 8 and 24 are evaluated. In order to preserve the east–west symmetry of the receiver flow paths, and facilitate off-design operations, only even bank numbers are considered. For each bank number configuration, the velocity for every possible configuration with an even number of flow paths is evaluated using Eq. (2). The configuration selected for each design is one that respects both the minimum and maximum flow velocity thresholds and has the minimum number of

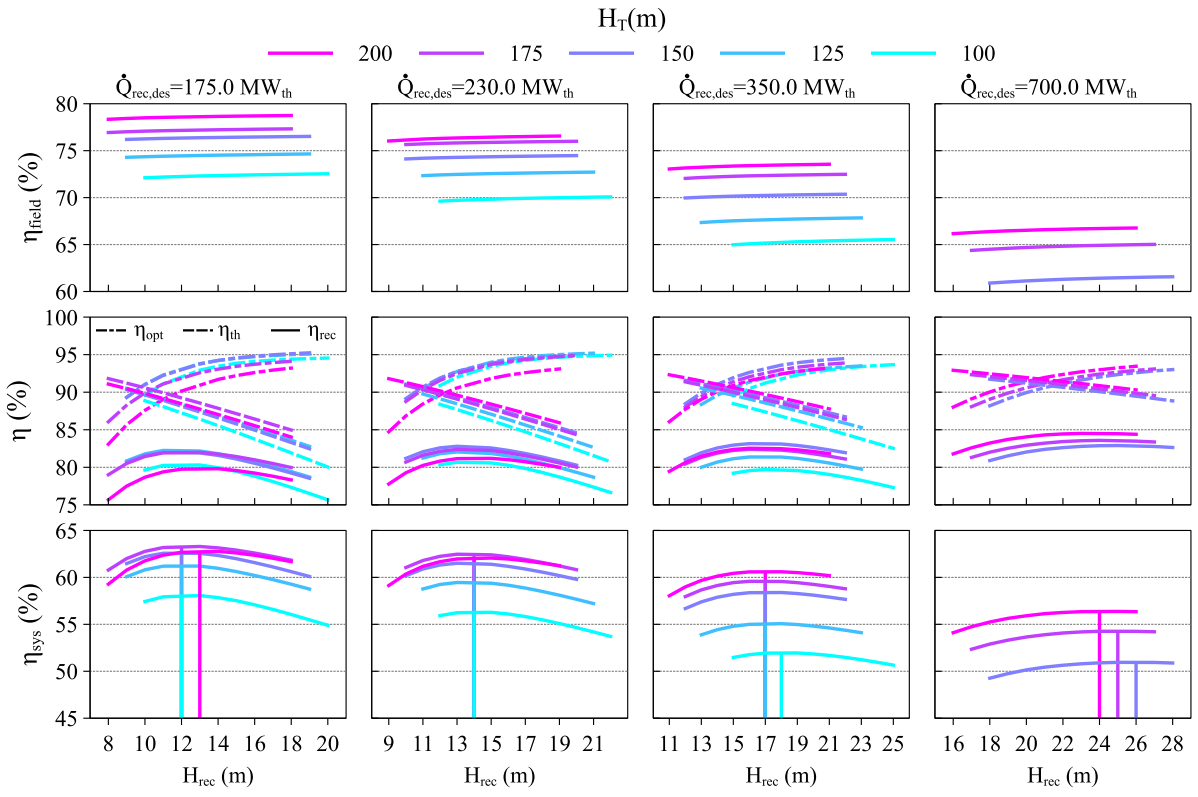

Fig. 3. Height design parametric study for all the configurations selected from the first stage. (For interpretation of the references to colour in this figure legend, the reader is referred to the web version of this article.)

banks and the minimum number of flow paths with this number of banks.

Once the number of banks and flow paths are determined for each configuration, a generic aiming strategy is established using the base settings of the MDBA method [26]. These settings do not provide an optimal aiming strategy but can reliably estimate spillage and concentration at the receiver, leading to reasonable efficiency estimations, as presented in the original work. The result of design point (equinox solar noon) simulations are shown in Fig. 3 with the following efficiency metrics:

- $\eta_{rec,opt}$ is the optical efficiency, which is the ratio of the absorbed power to the radiative power incoming in the vicinity of the receiver (before accounting for spillage effects and after atmospheric attenuation).
- $\eta_{rec,th}$ is the ratio of the net heat rate gained by the HTF to the absorbed power.
- $\eta_{rec} = \eta_{rec,opt}\eta_{rec,th}$ is the ratio of the net heat rate gained by the HTF divided by the radiative power incident in the vicinity of the receiver.
- η_{field} is the ratio of the radiative power incident in the vicinity of the receiver to the radiative power incident on the field aperture. η_{field} excludes spillage effects which are counted in $\eta_{rec,opt}$.
- $\eta_{sys} = \eta_{rec,opt}\eta_{field}$ is the ratio of net heat rate gained by the HTF to the radiative power incident on the field aperture.

As can be seen in Fig. 3, for each system design thermal capacity, the optical efficiency increases with receiver size as spillage is reduced. The diameter of each configuration has been fixed previously and the increase in receiver height translates into a linear increase in receiver surface area and a near-linear thermal efficiency drop. Opposite trends in optical and thermal efficiency give rise to a maximum receiver efficiency and corresponding receiver design height for each configuration. Field efficiencies for each tower height are fairly insensitive to receiver height but strongly depend on tower height, as has already been extensively studied in the literature [8]. The receiver height that is ultimately selected for each tower height evaluated maximises the receiver efficiency. As the field efficiency appears quasi-independent of the receiver height, the simplified design method, is expected to introduce minimal approximations in determining these two parameters sequentially.

Systems with smaller receiver design thermal capacity benefit from higher receiver optical efficiency while the largest system suffers from a significant optical efficiency penalty due to larger spillage. Receiver thermal efficiencies are higher for larger systems. Field efficiencies decrease with increasing system capacity mostly driven down by higher cosine and atmospheric attenuation losses. Overall, system efficiency decreases as system design capacity increases. An interesting observation is that the use of two systems instead of one can potentially result in significant system efficiency increases, enabled by a combination of higher field efficiency and optical efficiency of the receiver, both of which are purely optical factors.

2.3. Annual performance lookup tables

Annual performance evaluation is evaluated to generate Levelised Cost Of Electricity (LCOE) estimates from these designs. The model based on detailed ray-tracing and receiver energy balance is too computationally expensive to run for every time point evaluated in an annual performance model. Instead, reduced-order models are established based on annual performance lookup tables and transferred to a dynamic system analysis model based on the SolarTherm library [27] and presented in the following section. Two lookup tables are produced: one for the optical efficiency of the field at different sun positions, and one for the receiver thermal losses as a function of the thermal input, wind speed and ambient temperature.

2.3.1. Optical efficiency lookup tables (OELT)

The optical efficiency lookup table is established using a regular sun position sampling of 25 h angles and 7 declination angles at which the full system is simulated using the detailed model. The DNI is obtained from the clear-sky DNI model from [28] as implemented in PVlib from Sandia National Laboratories [29]. The OELT is used by the solar field model presented in 2.4.3 to compute the receiver input power. The simplified method using the OELT has been verified in a previous study [30,31], which demonstrated that the difference of the annual optical efficiency using the full-year detailed model and the OELT is less than 0.1%.

2.3.2. Receiver losses lookup table (RLLT)

The receiver losses lookup table is established based on a specific selection of representative days. First, the time periods from the Typical Meteorological Year (TMY3) data file with DNI values below 450 W/m^2 are ignored as the system is not able to operate under such low DNI levels. The system is assumed to be unable to operate until 45 min after sunrise and 45 min before sunset due to highly degraded field optics. Finally, days with less than one hour of minimum load of daily available DNI (i.e. 1.6 kWh) are ignored as well. From the remaining operable days, the days with minimum, maximum, and median daily averaged DNI, wind speeds, and ambient temperatures are selected and simulated with the full detailed model and with an hourly frequency. From these simulations, the average receiver external temperature, the average receiver external temperature to the fourth power, and the external convective heat transfer coefficient are recorded at each time point, along with the corresponding ambient temperature, incident radiative power from the field, and wind speed. These parameters are used in the receiver reduced-order model presented in 2.4.4.

2.4. System model

A CSP plant system model, developed by integrating the models of individual CSP components to simulate dynamic operations and annual performance, is implemented using the Modelica Standard Library (MSL) and available as part of the open-source library SolarTherm. SolarTherm consists of two core parts: a collection of Modelica classes with CSP component models, and a set of Python scripts to compile the models, execute simulations and optimisations, and post-process the results from the simulation. SolarTherm is typically used to calculate metrics like LCOE, capacity factor, revenue, and annual electrical output. Each component model is imported as an object into the system-level model, where it interacts with other models using connectors allowing the Modelica engine to solve the coupled equations that describe the system at each time step.

2.4.1. Weather data source

The SolarTherm `DataTable` class imports the hourly solar resource and meteorological data from a TMY3 file and interpolates the DNI, ambient temperature, atmospheric pressure, and wind speed throughout the annual simulation to make it available to the other models through `RealInput` connectors.

2.4.2. Sun model

The `Sun` model simulates the sun position by calculating the solar angles for each time step via the PSA algorithm from Blanco-Muriel et al. [32]. The `Sun` class transfers the DNI and solar angles data to the `HeliostaField` class via a `SunPort` connector to calculate the energy reflected and concentrated on the surface of the receiver.

2.4.3. Solar field

The `HeliostatField` model computes the raw field output ($\dot{Q}_{\text{field,raw}}$) from Eq. (7) as the product of total mirror area (A_{field}), direct normal irradiance (G), heliostat availability (η_{av}) and field optical efficiency (η_{opt}).

$$\dot{Q}_{\text{field,raw}} = G \cdot A_{\text{field}} \cdot \eta_{\text{av}} \cdot \eta_{\text{opt}} \tag{7}$$

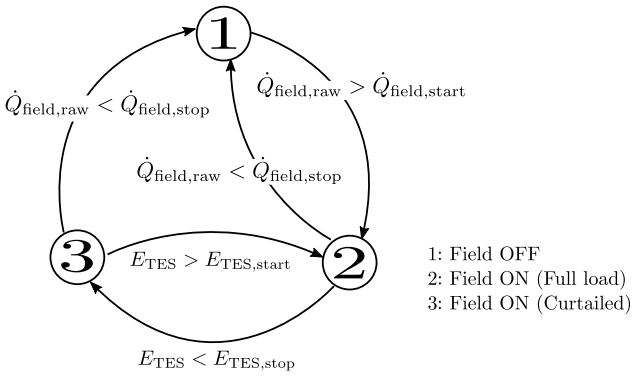

Fig. 4. Field operation states based on the raw field output and the field and storage operation thresholds.

Given solar angles, provided by the `Sun` connector, the model uses the MSL class `CombiTable2D` and Akima splines [33] to interpolate $\eta_{\text{field,opt}}$ from the optical efficiency lookup tables (OELT) with solar declination (δ) and hour (ω) angles as inputs.

In the dynamic annual simulation, the field thermal output is adjusted by the following operation thresholds:

- The solar field operates only when the elevation angle (α) is above 8°.
- The power necessary to start ($\dot{Q}_{\text{field,start}}$) the receiver is 25% of the design point receiver thermal input.
- The power threshold to shut-down ($\dot{Q}_{\text{field,stop}}$) the receiver is 20% of the design point receiver thermal input.
- The maximum wind speed to operate the field is 15 m/s.
- The field is curtailed when storage tanks are full and limited to a value that limits the output of the receiver such that it can run the power block at full capacity. The model determines the curtailed output from power block input and off-design receiver efficiency:

$$\dot{Q}_{\text{field,curtail}} = \min\left(\dot{Q}_{\text{field,raw}}, \frac{\dot{Q}_{\text{PHX}}}{\eta_{\text{rec}}}\right) \tag{8}$$

The transition between the operation states is depicted in Fig. 4 and net field output ($\dot{Q}_{\text{field}}$) is computed as:

$$\dot{Q}_{\text{field}} = \begin{cases} 0, & \text{State 1} \\ \dot{Q}_{\text{field,curtail}}, & \text{State 3} \\ \dot{Q}_{\text{field,raw}}, & \text{State 2} \end{cases} \tag{9}$$

Finally, $\dot{Q}_{\text{field}}$ is provided to the receiver model via a `HeatPort` connector.

2.4.4. Receiver

The `SodiumReceiver` class models the performance of the sodium receiver based on $\dot{Q}_{\text{field}}$, the ambient temperature and the wind speed through the solution of the energy balance in Eq. (10).

$$\alpha_{\text{eff}} \cdot \dot{Q}_{\text{field}} - \dot{Q}_{\text{rec,loss}} = \dot{m}_{\text{rec}} \cdot \left(h_{\text{rec,out}} - h_{\text{rec,in}}\right) \tag{10}$$

Within the model, receiver thermal losses ($\dot{Q}_{\text{rec,loss}}$) are obtained from Eq. (11) from instantaneous emission losses ($\dot{Q}_{\text{loss,emi}}$) and convection losses ($\dot{Q}_{\text{loss,conv}}$).

$$\dot{Q}_{\text{rec,loss}} = \dot{Q}_{\text{loss,conv}} + \dot{Q}_{\text{loss,emi}} \tag{11}$$

Convection losses are computed in Eq. (12) from average surface temperature ($\bar{T}_{\text{w}}$) and convective heat transfer coefficient (h_{conv}), which are interpolated based on the RLLT data using polynomial mapping functions with $\dot{Q}_{\text{field}}$, T_{amb} and v_{wind} as input variables [30,31]. The

model calculates $\bar{T}_w$ using a first-degree polynomial, while a fourth-degree polynomial function is required to compute h_{conv}.

$$\dot{Q}_{loss,conv} = h_{conv} \cdot A_{rec} \cdot \left(\bar{T}_w - T_{amb}\right) \tag{12}$$

Emission losses are evaluated with Eq. (13) from the average of the fourth-degree surface temperature ($\bar{T}'_w$), again interpolated from RLLT using polynomial regression, as well as $\dot{Q}_{field}$, T_{amb} and v_{wind} as inputs.

$$\dot{Q}_{loss,emi} = \epsilon_{eff} \cdot \sigma \cdot A_{rec} \cdot \left(\bar{T}'^4_w - T^4_{amb}\right) \tag{13}$$

The model estimates the parasitic power loss due to pumping sodium to the top of the tower with Eq. (14).

$$\dot{W}_{rec,pump} = \frac{\dot{m}_{rec}}{\bar{\rho}_{HTF} \cdot \eta_{pump}} \left(\Delta P_{rec} + \bar{\rho}_{HTF} \cdot g \cdot H_{tower}\right) \tag{14}$$

Finally, the `SodiumReceiver` class provides sodium mass flow rates and enthalpies to the sodium/salt heat exchanger model via `FluidPort` connectors.

2.4.5. Sodium-salt heat exchanger

The `HX` class models a shell and tube heat exchanger to simulate the heat transfer between sodium and chloride salt assuming negligible heat losses to the environment. The heat transfer rate is calculated from Eq. (15) and it is used to solve the steady-state energy balances in Eqs. (16) and (17).

$$\dot{Q}_{hx} = U A \cdot \Delta T_{LMTD} \tag{15}$$

$$\dot{Q}_{hx} = \dot{m}_{rec} \cdot \left(h_{rec,out} - h_{rec,in}\right) \tag{16}$$

$$\dot{Q}_{hx} = \dot{m}_{hx,salt} \cdot \left(h_{salt,out} - h_{salt,in}\right) \tag{17}$$

The heat exchanger design is based on Guccione et al. [34]. From this model, the shell-side (i.e. salt side) and the tube-side (i.e. sodium side) pressure drops are estimated and used to determine the pumping power required to maintain the sodium and the salt mass flow rates.

2.4.6. Riser and downcomer

The liquid sodium riser and downcomer designs are estimated through detailed thermal insulation analyses using heat loss coefficients from ASTM C 680 - 89 and ASME B31.3 design guidelines (K < 0.003 rule) to size the thermal expansion loop and the thickness of the pipe, similarly to Turchi et al. [6]. The expansion loops have a length of 3 m perpendicular to the pipe run and an aspect ratio of 2 (leading to 1.5 m in the direction of the pipe run). The design pressure was estimated by adding 1 bar to the hydrostatic head from the top of the receiver to the bottom of each tower, which accounts for receiver pipe banks pressure drops (<0.5 bar) and all other flow disturbances from accessories in expansion loops, valves, headers, etc.

2.4.7. Thermal energy storage

The `Tank` class from SolarTherm simulates the time-dependent behaviour of a sensible heat thermal energy storage (TES).

Within the `tank` class, mass and energy balances are modelled as in Eqs. (18) and (19).

$$\frac{d m_{TES}}{dt} = \dot{m}_{TES,in} - \dot{m}_{TES,out} \tag{18}$$

$$\frac{d E_{TES}}{dt} = \dot{Q}_{TES,loss} + \dot{Q}_{TES,aux} + \dot{m}_{TES,in} \cdot h_{TES,in} - \dot{m}_{TES,out} \cdot h_{TES,out} \tag{19}$$

Convective losses to the environment ($\dot{Q}_{TES,loss}$) are obtained from Eq. (20), with a fixed heat loss coefficient ($h_{conv,TES} = 0.45\ \mathrm{W/m^2\ K}$) from [6].

$$\dot{Q}_{TES,loss} = -h_{conv,TES} \cdot A_{TES} \left(T_{TES} - T_{amb}\right) \tag{20}$$

The tank model considers an auxiliary heat supply ($\dot{Q}_{TES,aux}$) to maintain the tank set-point temperature defined by the user. The heater power is controlled to perfectly offset the calculated thermal losses from the tank but is constrained by an upper bound specified in the model (30 MW for the hot tank, and 15 MW for the cold tank). The power consumption of the heater is calculated according to an efficiency value ($\eta_{aux} = 99\%$), which is provided as a parameter.

2.4.8. Power block

The `SurrogatesCO2PB_OTF` class models the performance of the sCO_2 recompression Brayton power cycle by running off-design calculations of the thermal input and gross power output of the cycle.

The instantaneous gross power output ($\dot{W}_{gross}$) is obtained from the instantaneous thermal input and the off-design thermal efficiency (η_{PB}) in Eq. (21), which accounts for the effect of the off-design salt flow rate and temperature at the primary heat exchanger (PHX) inlet, and ambient temperature.

$$\dot{W}_{gross} = \dot{Q}_{PHX} \cdot \eta_{PB} \tag{21}$$

The instantaneous thermal input ($\dot{Q}_{PHX}$) to the power block primary heat exchanger (PHX) is computed in Eq. (22)

$$\dot{Q}_{PHX} = \dot{Q}_{PHX,des} \cdot \eta_q \tag{22}$$

where $\dot{Q}_{PHX,des}$ is the PHX design thermal rating and η_q is the off-design thermal fraction, a dimensionless factor that accounts for the effect of the off-design salt flow rate and temperature, and ambient temperature on the thermal input of the power block.

The `SurrogatesCO2PB_OTF` model obtains $\dot{Q}_{PHX,des}$ from the cycle nominal power by running the detailed on-design simulations using the model from [35], embedded in the SAM Simulation Core (SSC).

The values of η_q and η_{PB} are calculated via an external Python subroutine that executes a surrogate model. The details of the equations and training of the surrogate model are presented in Appendix A.

Finally, the `SurrogatesCO2PB_OTF` model also determines the salt enthalpies by solving the energy balance in Eq. (23).

$$\dot{Q}_{PHX} = \dot{m}_{PHX,salt} \cdot \left(h_{salt,PHX,out} - h_{salt,PHX,in}\right) \tag{23}$$

The system net power output depends on the gross power output, the base parasitic loss ($\dot{W}_{par,base}$), the variable parasitic losses ($\dot{W}_{par,var}$) and the cooling power ($\dot{W}_{par,cool}$) :

$$\dot{W}_{net} = \dot{W}_{gross} - \dot{W}_{par,base} - \dot{W}_{par,var} - \dot{W}_{par,cool} \tag{24}$$

The base parasitic loss ($\dot{W}_{par,base}$) – a fixed electric load consumed on building loads, lighting, and other loads – is set to 0.5% of the design heat input ($\dot{Q}_{PHX,des}$). The variable parasitic loss accounts for the operation of the pumps, the heliostats and the power supply from the TES auxiliary heaters:

$$\dot{W}_{par,var} = \dot{W}_{par,hel} + \dot{W}_{par,pumps} + \dot{W}_{TES,aux} \tag{25}$$

where the power losses due to heliostat tracking ($\dot{W}_{par,hel}$) is the accumulation of tracking power of active heliostats, assuming each heliostat tracking device consumes 55 W while the field is on NREL [36]. The power loss due to auxiliary heating ($\dot{W}_{TES,aux}$) accounts for the power loss due to electric heaters used to prevent the salt temperature from dropping below the TES temperature set-points.

The total power loss due to pumping is obtained as:

$$\dot{W}_{par,pumps} = \dot{W}_{Na,pump} + \dot{W}_{salt,pump} + \dot{W}_{PB,pump} \tag{26}$$

where $\dot{W}_{Na,pump}$, $\dot{W}_{salt,pump}$ and $\dot{W}_{PB,pump}$ accounts for the pumping power of the sodium pumps, the cold-tank pump, and the hot-tank pump, respectively. Each individual power consumption is calculated as the product of a pump-specific parasitic power coefficient (k_{loss}) and the corresponding mass flow rate. The values for k_{loss} are 22 W/(kg/s) for the sodium pump, 150 W/(kg/s) for the cold-tank pump, and 550 W/(kg/s) for the hot-tank pump.

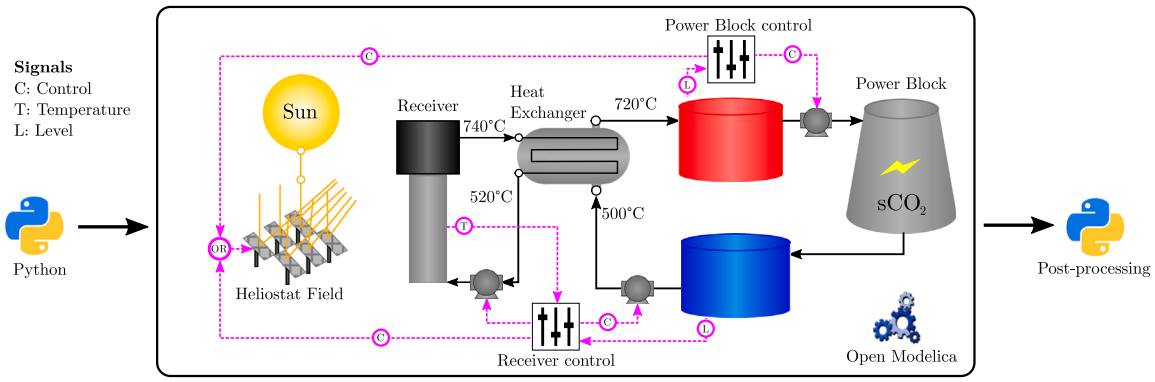

Fig. 5. Graphical representation of the system-level model to simulate the numbered-up configurations in SolarTherm.

2.5. Annual simulation methodology

A graphical representation of the SolarTherm model, from the GUI of the software, is shown in Fig. 5.

High-level parameters are set for each configuration within the plant model, i.e. net power output, tower height, thermal receiver size, and full-load hours of storage. Once the simulation starts, SolarTherm adjusts the remaining parameters, calculates capital investment, and imports the OELT, RLLT and TMY files. At each time step, the system model interpolates the DNI, wind speed, ambient temperature and calculates the solar angles to provide inputs to the individual components and determine time-dependent operation variables, i.e. temperatures, pressure, enthalpies, mass flow rates, tank levels and heat transfer rates, among others.

Two control components manage the operation of the plant. The power block control system uses the level of the hot tank to prescribe a mass flow rate for the salt at the power block inlet. If the hot tank is empty, the control system will stop the discharge. The receiver control system prescribes the discharge mass flow rate of the cold tank depending on the tank filling level. If the tank is empty, the control system will stop the discharge and flag a defocus signal to the field to prevent an increase in the receiver outlet temperature.

Whenever the cold or hot tanks are full, the controllers will flag a defocus signal to the heliostats field to reduce the heat input to the system. The defocus heat rate is the required heat to run the power block at nominal conditions.

2.6. SolarTherm verification

A verification of the SolarTherm results was performed via comparison with the System Advisor Model (SAM) from NREL [37]. An alternative full system model using a single HTF, a chloride ternary salt, throughout the receiver and storage system was selected due to limitations in simulating a dual fluid system in SAM. While it is not possible to include full details of this validation case due to space constraints in this paper, the comparison between the performance and LCOE obtained with the two software is presented in Table 4 and shows that differences in the annual receiver output and net electrical power output are ±1.8% and ±1.4%, respectively. Differences in the LCOE calculation are within ±1.0%. More details of the verification are presented in the study carried out by Fontalvo et al. [38].

SAM uses a 1-hour time step within its built-in solver during the annual simulation. The SolarTherm model employs a differential/algebraic system solver (DASSL) with an implicit backward differentiation formula (BDF) with simulation steps of 5 min. This feature enables SolarTherm to better handle control decisions for processes lasting less than 1 h, such as receiver start-ups, shutdowns, and field curtailment.

Table 4
Verification of the annual performance metrics and LCOE obtained from SolarTherm when compared to SAM for an equivalent high-temperature salt system [38].

Parameter	SAM	SolarTherm	Difference
Annual energy yield (GWh_e)	551.6	559.1	1.36%
Capacity factor (%)	63.0	63.9	0.89%
LCOE (USD/MWh_e)	79.3	78.6	−0.95%
Annual field efficiency (%)	49.8	50.8	1.05%
Annual plant efficiency (%)	16.8	17.2	0.42%
Annual rec. input (GWh_{th})	1,635	1,651	0.99%
Annual rec. output (GWh_{th})	1,261	1,238	−1.80%
Parasitic loss (GWh_e)	36.1	36.6	1.39%

2.7. Techno-economic model

Finance and cost data are compiled from a range of sources, including direct contact with industry partners, public reports, and, where applicable, DOE reference values (e.g., for heliostats). Table 5 summarises the key financial and cost inputs. The SolarTherm implementation adjusts various values (where indicated) so that they are appropriate to each plant scale by using power-law relationships.

This study assumes a cost reduction due to multiple units for modular systems, considering a lower price per unit when two or more identical components are purchased. The model applies this discount to all CSP component costs except the field and site improvement costs. The amount that cost was discounted for each numbering-up case was determined through a survey of industry partners. These amounts are 16% for four components of the same type, 14.5% for three, and 11% for two. Finally, the storage tanks are the only CSP components with a discount in the 100 MW_e system. This study assumes two pairs of storage tanks for the 100 MW_e due to limitations in building large storage tanks [6].

In this study, a conservative approach was taken for the cost of towers, assuming a reinforced concrete construction where receiver size and mass do not affect the tower cost and adopting the costing equation from the SAM software [36]:

$$C_{\text{tower}} = C_{\text{tower,fixed}} \cdot \exp\left(a \cdot H_{\text{tower}}\right) \tag{27}$$

where $C_{\text{tower,fixed}}$ is fixed tower cost of 3 million USD, a is the scaling exponent of 0.0113, and H_{tower} is the tower height. The expression above includes the cost of tower construction, materials and labour.

For the sodium receiver cost, this study adopted a relationship that adjusts the costs depending on the size or capacity of the receiver, based on the approach taken by Kelly [39] and arguing that increases in diameter would require more additional welds and tubes, while taller receivers would simply require longer tube lengths. The resulting scaling expression is presented in equation Eq. (28), where $C_{\text{rec,fixed}}$ is a fixed cost for engineering and $C_{\text{rec,ref}}$ is a size-dependent reminder of cost for a reference case. Receiver cost is scaled linearly with diameter

Table 5
Financial and cost inputs for LCOE calculations.

Cost input	Unit	Reference value	25 MW_e module	33 MW_e module	50 MW_e module	100 MW_e module	Notes and sources
Parameters for optimum LCOE							
Receiver thermal input[a]	MW_{th}	–	175	230	350	700	–
Receiver thermal output[a]	MW_{th}	–	154	199	309	628	–
Receiver diameter[a]	m	–	10	12	13	17	–
Receiver height[a]	m	–	12	14	17	25	–
Tower height[a]	m	–	100	100	125	175	–
Riser diameter[a,b]	m	–	0.508	0.559	0.66	0.66	–
Downcomer diameter[a,b]	m	–	0.508	0.559	0.66	0.66	–
Financial assumptions							
Periods	years	30	30	30	30	30	DOE [19]
Discount rate, real[c]	%	4.4	4.4	4.4	4.4	4.4	DOE [19].
Fixed O&M costs	USD/kW-y	40	40	40	40	40	DOE [19]
Variable O&M costs	USD/MWh_e	3	3	3	3	3	DOE [19]
Contingency	%	10	10	10	10	10	Applied to all costs [19].
EPC/owner cost	%	9	9	9	9	9	Applied to all direct costs [19].
Land cost	USD/acre	10,000	10,000	10,000	10,000	10,000	DOE [19]
Heliostat Field							
Site improvements	USD/m^2	10	10	10	10	10	DOE 2020 SunShot target [18].
Heliostats	USD/m^2	75	75	75	75	75	DOE 2020 SunShot target [18].
Sodium Receiver							
Fixed cost component	M.USD	4.78	4.78	4.78	4.78	4.78	Fixed cost for engineering from [39], adjusted for inflation, then increased 9.5% for 740H materials in header and piping, additional insulation, heat trace, post-weld heat treatment, and includes receiver insulation.
Size-dependent cost component	M.USD	35.40	13.70	18.03	21.94	36.17	Size-dependent cost based on proprietary information from the Atacama/John Cockerill receiver, inflation-adjusted and increased by 9.5% as above.
Tower							
Tower cost	M.USD	–	9.29	9.29	12.32	21.67	Values from Eq. (27).
Sodium Loop							
Sodium valves[d]	M.USD	1.27	0.51	0.81	1.11	1.82	Valves are already included in the receiver costing listed above. This line item is an allowance to account for additional valves due to additional flow paths, estimated as half the valve cost in the SolarReserve APOLLO report [40].
Sump tank[e]	M.USD	2.07	0.70	0.84	1.15	1.89	Farinelle [41]
Inlet vessel[e]	M.USD	0.36	0.12	0.15	0.20	0.33	Farinelle [41]
Purification skid[e]	M.USD	0.49	0.17	0.20	0.27	0.45	Farinelle [41]
Sodium pumps[f]	M.USD	5.48	2.12	2.56	3.48	5.72	Reference is based on 4 × 33% pumps at €1,121,977 per pump, with costs taken from a Budget Quotation from Sulzer for a cold salt pump, for the 543 MW_{th} salt pathway down-selection case. The casing, impeller & shaft are Inconel 625. The pump manometric head is 270 m. Flow is 1064 m^3/h per pump. Pumps have 4 stages.
Argon system[e]	M.USD	0.14	0.06	0.07	0.09	0.13	Farinelle [41]
Instrumentation & Control[d]	M.USD	0.42	0.22	0.25	0.31	0.44	Farinelle [41]
Additional piping allowance[e]	M.USD	2.00	0.67	0.81	1.11	1.82	Most piping costs in the receiver are covered by the Atacama/John Cockerill receiver reference cost. This is an additional allowance for larger diameter piping.
Sodium and Salt Piping							
Sodium riser/cold salt piping material cost[j]	USD/kg	8	8	8	8	8	Material is UNS S31600.
Sodium downcomer/hot salt piping material cost[j]	USD/kg	80	80	80	80	80	Material is UNS N07740.

(*continued on next page*)

Table 5 (*continued*).

Sodium riser/cold salt piping balance of costs[g]	USD/m	5595	3996	4398	5192	5192	Reference value excludes piping material but includes insulation, trace heat, installation, welds, wastage, freight, materials handling, testing and inspection, hangers and supports.
Sodium downcomer/hot salt piping balance of costs[g]	USD/m	8502	6073	6683	7890	7890	As above for the riser, but costs of insulation, heat trace, fittings revised in Section 2.7 to account for the higher temperature.
Thermal Storage							
Tank and salt costs	USD/kWh$_{th}$	39.47	46.99	42.95	39.47	39.47	Values from NREL tank costing model [6]. Reference value set to a single tank pair, 12 h storage.
Salt (included above)	USD/kg	0.7	0.7	0.7	0.7	0.7	Delivered and melted salt based on prices from Israel Chemicals Limited (ICL).
Cold salt pump[f]	M.USD	3.99	1.55	1.87	2.54	5.14	Reference is based on 4 × 33% pumps at €818,498 per pump, with costs taken from a Budget Quotation from Sulzer for a hot salt pump at 543 MWth scale. Casing, impeller & shaft are Inconel 625. Reference pump manometric head is 87.2 m and flow is 1014 m^3/h.
Hot salt pump[f]	M.USD	3.00	1.16	1.40	1.91	3.85	Reference is based on 3 x 50% pumps at €818,498 per pump, with other details as for cold salt pump above.
Salt valves[h]	M.USD	2.11	1.18	1.42	1.93	3.91	Reference based on seven control valves, each 300,960 USD based on a 270 KUSD estimate by Flowserve for a 10″ globe valve with bellows seal made from 316H and adding an extra cost allowance for upgrading to a nickel alloy. Installation included with piping.
N_2 ullage gas system[i]	M.USD	2.86	2.86	2.86	2.86	5.72	Reference is for pilot scale ullage gas piping & installation scaled up for the number of pumps in the commercial scale, plus commercial-scale acid-gas scrubber, plus present value estimate for on-site N_2 production throughout 30-yr plant life.
Power Block and HEXs							
Sodium-salt HEX	USD/m^2	1834	2552	2352	2045	1642	Assumes a two-stage heat exchanger, (stainless steel and Inconel). Costs based on the John Cockerill sodium study from [41] but adjusted as described in [6].
Salt-CO_2 PHX	USD/kW$_{th}$	229	229	229	229	229	Reference based on estimates from Vacuum Process Engineers (VPE), for 110 MWth, dual core unit. Low-temp core of stainless steel, high-temp core of alloy 617. Installation costs equal 21% of materials cost based on guidance from VPE as described in [6].
sCO_2 power block	USD/kW$_e$	600	909	834	739	600	Reference is from the Fig. 4 of the DOE funding opportunity announcement for a 100-MWe unit [42].

[a]System with fixed power block efficiency and minimum LCOE.
[b]Two sets of riser/downcomer piping for the 100 MW$_e$ module, one for the remaining modules.
[c]Converted to real from nominal using the Fisher equation, a 7.01% nominal discount rate, and 2.5% inflation from [19].
[d]Reference from the SolarReserve APOLLO report [40] at 565 MW$_{th}$.
[e]Reference from John Cockerill for their 720 MW$_{th}$ sodium receiver case study [41].
[f]Reference from the 543MW$_{th}$ salt pathway down-selection case.
[g]Reference value is based on the 28″ downcomer from [39].
[h]Reference value for the 350MW$_{th}$ receiver from [6].
[i]The cost of the N_2 ullage system is scaled linearly from the number of tank-pairs.
[j]Cost data from personal communication with John Cockerill.

D_{rec} relative to the reference receiver diameter D_{ref}, and using a power law relationship for height H_{rec}, relative to the reference height H_{ref}. The reference case is an external cylindrical receiver, with 'solar salt' as the working fluid and dimensions of 20-m diameter x 18.4-m high.

$$C_{rec} = C_{rec,fixed} + C_{rec,ref}\left(\frac{D_{rec}}{D_{ref}}\right)\left(\frac{H_{rec}}{H_{ref}}\right)^{0.6} \quad (28)$$

For the sodium loop systems, and salt pumps and valves, the cost of each component is estimated from reference cost data for specific receiver designs listed in Table 5. Each cost is scaled based on receiver thermal output using a power law with exponent 0.7 in all cases except for the argon and the instrumentation & control systems, which are assumed to have more fixed cost components and an exponent 0.5 is used.

For the sodium riser and downcomer, the cost of each piping system is estimated based on their length, diameter, and material employing the following expression:

$$C_{\text{piping}} = C_{\text{boc}} \left(\frac{D_{\text{pipe}}}{D_{\text{pipe,ref}}} \right) \cdot L_{\text{piping}} + C_{\text{pipe,mat}} m_{\text{piping}} \quad (29)$$

where C_{boc} is the reference balance-of-costs, $D_{\text{pipe,ref}}$ is the pipe diameter, $D_{\text{pipe,ref}}$ is the reference diameter, L_{piping} is the total piping length, $C_{\text{pipe,mat}}$ is the pipe material cost, and m_{piping} is the total piping mass, which is estimated from the piping length and the pipe cross-section area.

The reference costs are based on detailed information from [39] for the 28″ diameter, Schedule 20, SS347H downcomer from the Abengoa design. The balance-of-costs for the sodium riser are expressed in USD/m for the 28″ reference diameter as per Table 5, and assumed identical to the SS347H downcomer in the Abengoa study, given the similar operation temperature and dimensions. For the sodium downcomer, the balance-of-costs are revised upwards, multiplied by a factor of 1.5× for insulation, 4× for heat trace, and 1.05× for fittings, due to the higher operating temperature.

Pipe material costs are calculated directly for each case considering the piping material cost and the total piping mass. The riser/downcomer lengths (L_{piping}) are calculated from the tower height, a further 10-m horizontal distance, noting the heat exchanger is located close to the base of the tower, and a length scaling factor is applied to account for expansion loops, calculated as 1.43× for the sodium riser and 1.45× for the sodium downcomer.

The cost of the hot and cold salt piping is also determined using Eq. (29) with the reference costs and sizes listed in Table 5. The balance-of-costs, reference diameter, and pipe material costs for the cold salt piping are identical to the sodium riser, while the cost data for the hot salt piping is identical to the sodium downcomer. The hot/salt piping lengths are calculated from a 20-m horizontal distance from the heat exchanger to the tanks, and a further 10-m horizontal distance from the tanks to the power block. Similar to the riser and downcomer, a length scaling factor is applied to account for expansion loops, calculated as 1.43× for the cold salt piping and 1.45× for the hot salt piping.

The cost of the power block is estimated from reference cost per kW_e for a 100-MW_e unit, and scaled based on the power block capacity using a power law with exponent 0.7. For the power block salt/sCO_2 heat exchanger, the cost is scaled linearly from the reference cost of a 100-MW_{th} unit. Finally, the cost of the sodium/salt heat exchanger is estimated from the product of the heat exchanger area and the specific cost per m^2, which is scaled based on the heat capacity with an exponent of 0.7. All reference costs and sizes for the power block and heat exchangers are listed in Table 5.

It is important to point out that the cost considerations in this study are informed by the 2030 cost targets set by the Gen3 CSP programme [19]. Cost assumptions, like the one for the sCO_2 power block, are aligned with the projected cost reductions in the programme. Although these costs seem lower than current market rates for similar technologies, they reflect the targeted advancements and efficiencies. The authors acknowledge that these estimates may seem ambitious in the current context. Still, the analysis is focused on the long-term prospects and advancements in CSP technology with liquid-phase receivers. On the other hand, the cost assumption for chloride molten salts is somewhat conservative compared with recent studies that reported costs of 0.35 USD/kg [1] and less than 0.5 USD/kg [2]. These assumptions are in line with the long-term design considerations for CSP plants and aim to account for potential variability and market fluctuations in the cost of such materials.

3. Results

The LCOE of the systems presented in Section 2.2 is evaluated using the system model presented in Section 2.4. Based on experience from other types of power cycles, systems with lower design thermal capacity should suffer power block design efficiency de-rating. For sCO_2 power blocks, there is currently no publicly available data on the impact of the power block design capacity on the efficiency, partly due to the fact that there are no commercial sCO_2 power blocks operating yet. It is, therefore, difficult to estimate this impact reliably. This work first compares systems simulated assuming an identical power block design efficiency of 51% at all system design powers, and then repeat our simulations estimating the efficiency de-rating impact using information obtained within the framework of the DOE Gen3 Liquids pathway project, and presented in A.2. In addition, the multiple unit cost reduction factor (described above) implemented in the techno-economic model is a difficult factor to estimate and one that can influence the LCOE results significantly. In order to provide some perspective on the relative importance of this parameter, a sensitivity analysis is carried out in Section 3.3.

3.1. Configurations with fixed power block efficiencies

Fig. 6(a) and (b) show the optimum full load hours of storage and LCOE obtained for all configurations, respectively, and indicate that the numbering-up has very little impact on the optimal storage capacities with the optimal value lying in the 11.4 to 11.8 h range for all designs. The results also indicate that the effect of tower height on LCOE is scale-dependent. Fig. 6(b) shows that short towers (100 m) lead to the lowest LCOE for 25 MW_e modules but, as the scale increases, the optimum tower height increases. Systems with 33 MW_e modules have the lowest LCOE with 100 m high towers, similarly 125 m high towers for 50 MW_e modules and 175 m high towers for single-module 100 MW_e systems. In addition, the impact of tower height on LCOE decreases as the plant size increases. More details on the effect of full load hours of storage on LCOE can be consulted in Appendix B.

Table 6 lists the optimised configurations that minimise LCOE. The single-module 100 MW_e system with a 175 m high tower and 11.7 h of storage achieves the lowest LCOE (54.88 USD/MWh_e) and shows the highest capacity factor (81.2%). The system with two 50 MW_e modules and 100 m high towers includes the same storage capacity and achieves an LCOE of 55.99 USD/MWh_e, 2.0% higher, and a capacity factor of 79.2%. For smaller modules, the LCOE increases to 58.69 USD/MWh_e (+6.9%) and 61.56 USD/MWh_e (+12.2%), respectively, and the capacity factor drops to 78.0% and 77.5%, respectively.

Smaller systems have marginally higher annual optical field efficiencies, however, some of this advantage is lost after considering the annual operation of the receiver and storage, which is reflected in the solar-to-thermal and solar-to-electrical efficiencies shown in Fig. 7. The main reason for this drop is the smaller storage size obtained in the optimal configurations, which limits the power block operating hours. Furthermore, this constraint forces prolonged field curtailment during high-DNI days, penalising receiver output.

Fig. 8(a) presents the LCOE cost breakdown for the optimised systems in Table 6. The relative contributions of the power block (16.9–17.1%), salt piping and pumps (2.8–3.6%), sodium-salt heat-exchanger (3.7–4.1%) and storage system (13.5–14.0%) to the total cost do not change much with increasing system modularity. The solar subsystem shows the largest contribution to the total cost with the solar field and site improvements cost accounting for 13.6–16.5%, the receiver 10.4–12.7% and the tower 3.4–4.5% with a stronger dependence on system modularity.

3.2. Impact of power block efficiency de-rating

The annual simulations are repeated with power block efficiency de-rating and the results are shown in Fig. 6(c) and (d). The drop in

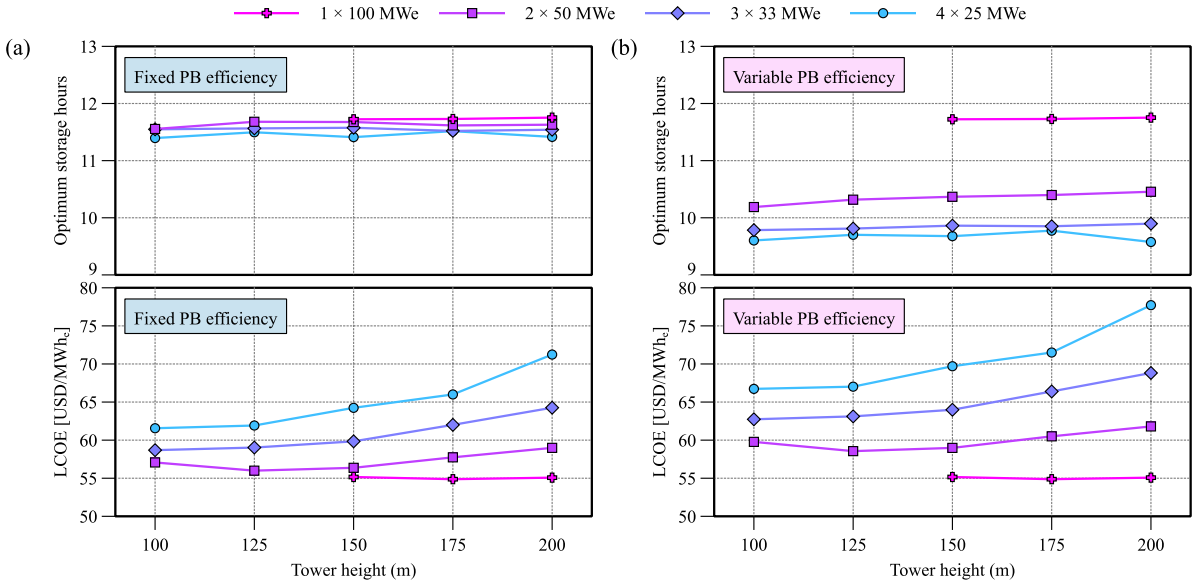

Fig. 6. Effect of tower height on the optimum full-load hours of storage and LCOE for numbered-up systems with (a) 51% fixed, and (b) scale-dependent design-point power cycle efficiency. (For interpretation of the references to colour in this figure legend, the reader is referred to the web version of this article.)

Table 6
Optimised numbered-up configurations that minimise LCOE with fixed power cycle efficiency.

Numbered-up system	Power block efficiency (%)	Receiver thermal input (MW_{th})	Receiver thermal output (MW_{th})	Tower height (m)	Storage capacity (h)	Annual output (GWh_e)	Capacity Factor (%)	LCOE (USD/MWh_e)
4 × 25 MW_e	51.0	175	152	100	11.4	677.1	77.3%	61.56
3 × 33 MW_e	51.0	230	199	100	11.5	683.0	78.0%	58.69
2 × 50 MW_e	51.0	350	309	125	11.7	693.4	79.2%	55.99
1 × 100 MW_e	51.0	700	628	175	11.7	711.1	81.2%	54.88

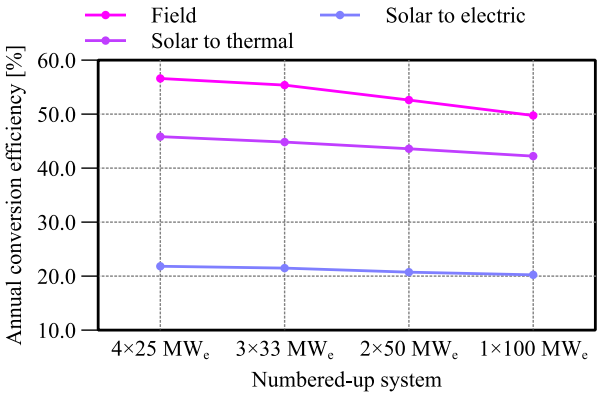

Fig. 7. Annual conversion efficiencies for the optimised systems. Fixed power cycle efficiency. (For interpretation of the references to colour in this figure legend, the reader is referred to the web version of this article.)

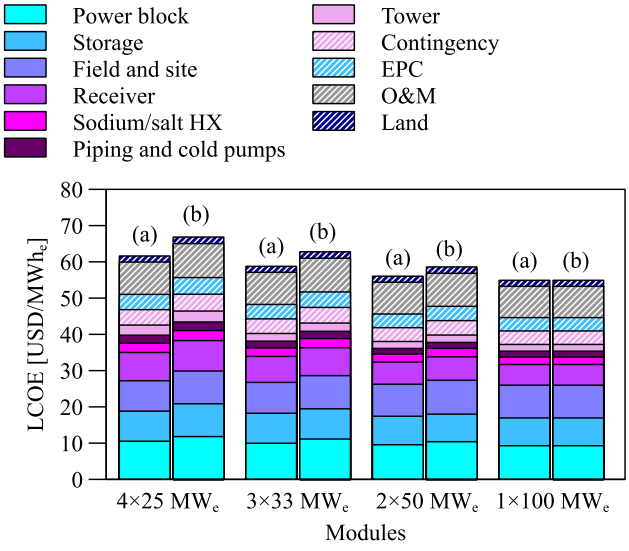

Fig. 8. LCOE breakdown for optimised numbered-up systems with (a) fixed and (b) scale-dependent power block efficiency. (For interpretation of the references to colour in this figure legend, the reader is referred to the web version of this article.)

power block efficiency for smaller systems has an impact on the optimal storage size and causes the lowest LCOE systems to have smaller storage systems, in the 9.6–10.5 h range, irrespective of tower height. Fig. 6(c) shows that the optimal tower heights remain identical to the results of the previous section showing that the power block efficiency de-rating does not influence the optimal tower height significantly.

The optimal systems obtained with scale-dependent power cycle efficiencies are listed in Table 7. As in the previous section, the LCOE increases with decreasing power plant design capacity, however, the power block efficiency reduction causes an additional LCOE increase of 4.6% for the 50 MW_e modules, 6.9% for the 33 MW_e modules and 8.4% for the 25 MW_e modules. As the thermal design power at the receiver is fixed, the power block efficiency reduction causes a reduction in capacity factor for the numbered-up configurations. The resulting LCOEs are now 6.7% higher than the single 100 MW_e system for the two 50 MW_e modules while it is 14.3% for the three 33 MW_e modules and 21.6% for the four 25 MW_e modules. More details on the effect of full load hours of storage on LCOE can be consulted in Appendix B.

Table 7
Optimised numbered-up configurations that minimise LCOE with scale-dependent power cycle efficiency.

Numbered-up system	Power block efficiency (%)	Receiver thermal input (MW_{th})	Receiver thermal output (MW_{th})	Tower height (m)	Storage capacity (h)	Annual output (GWh_e)	Capacity Factor (%)	LCOE (USD/MWh_e)
4 × 25 MW_e	45.6	175	152	100	9.6	628.6	71.8%	66.73
3 × 33 MW_e	46.3	230	199	100	9.8	635.3	72.5%	62.74
2 × 50 MW_e	47.6	350	309	125	10.3	655.6	74.8%	58.56
1 × 100 MW_e	51.0	700	628	175	11.7	711.1	81.2%	54.88

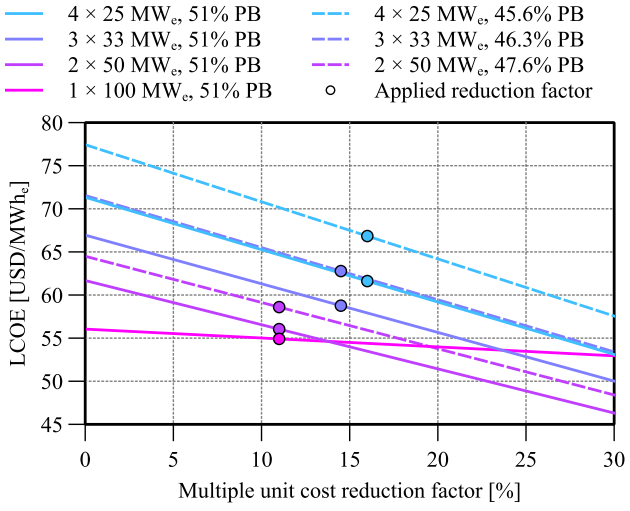

Fig. 9. Effect of multiple unit discount on LCOE for optimised numbered-up systems. (For interpretation of the references to colour in this figure legend, the reader is referred to the web version of this article.)

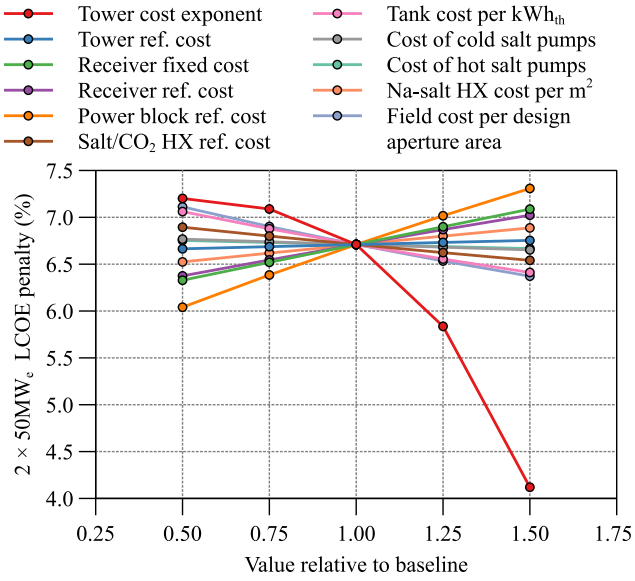

Fig. 10. Sensitivity of the LCOE penalty for the optimised 2 × 50 MW_e configuration to variations in the costs of various components. (For interpretation of the references to colour in this figure legend, the reader is referred to the web version of this article.)

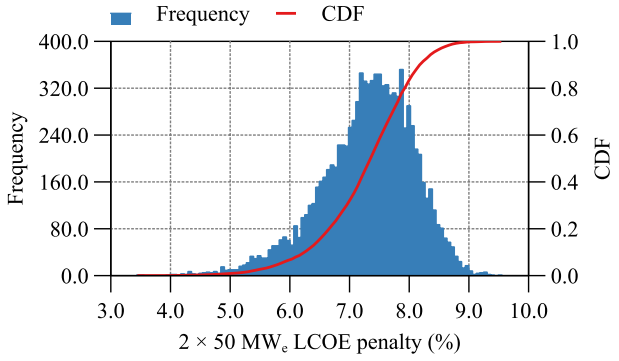

Fig. 11. Sensitivity of the LCOE penalty for the optimised 2 × 50 MW_e configuration to variations in the costs of various components.

The specific LCOE breakdown for the optimised systems with de-rated power block efficiency is presented in Fig. 8(b). These results show that by decoupling the effect of the power cycle efficiency, the improvement in the performance of the field-receiver subsystem compensates for the increase in costs due to the use of small-scale modules. It becomes evident when comparing the 100 and 50 MW_e modules, where small-scale modules come with a minor penalty of ≈2.1%. However, once the efficiency effect is incorporated, the difference widens to 6.7%.

3.3. Impact of multiple unit cost reduction

Parametric analysis on the effect of multiple unit cost reduction factor on LCOE is carried out for the best 50 MW_e and 100 MW_e systems.

Fig. 9 shows how the variations between 0 and 30% in multiple unit discount has a more significant impact on the LCOE of small-scale modules than in the large scale system with and without capacity-dependent efficiency. Results also indicate that numbered-up systems with 50 MW_e modules could achieve lower LCOEs than large-scale 100 MW_e systems if a cost reduction factor of 13.9% is applied. This factor depends on the power block efficiency. On the other hand, Fig. 9 shows that the drop in power block efficiency reduced the techno-economic performance of small-scale modules, and the discount threshold, where these systems had lower LCOE than large-scale systems, is pushed to 19.6%.

3.4. Sensitivity of LCOE to component cost

A sensitivity analysis of the difference in LCOE between the optimised 2 × 50 MW_e and 1 × 100 MW_e configurations is performed. Within this analysis, the LCOE of these optimised configurations is re-calculated after the application of a ±50% variation in the cost parameters from Section 2.7. The LCOE penalty

$$2{\times}50\,\mathrm{MW_e}\ \mathrm{LCOE\ penalty} = \left(\frac{\mathrm{LCOE_{50}}}{\mathrm{LCOE_{100}}} - 1\right) \cdot 100\% \tag{30}$$

rather than the LCOE itself is the focus of this sensitivity analysis, providing a more targeted assessment of the impact of component cost variations on the difference between the two optimised configurations.

Fig. 10 illustrates that the LCOE penalty is sensitive to changes in these costs. Nonetheless, the degree of sensitivity varies among the components and the extent of their adjustments.

Lastly, Fig. 11 shows the result of a constrained Monte-Carlo sensitivity analysis when all cost assumptions are considered simultaneously. The samples were generated using the Latin Hypercube Sampling

(LHS) method [43] embedded in the Dakota software [44] by assuming a triangular probability distribution. As a result, the probable LCOE penalty distribution is skewed slightly towards LCOE values above the nominal result of 6.71%, but absolute variations in LCOE penalty remain within a 10% range. In particular, parameters such as the 'Tower cost exponent', 'Power block reference cost', and 'Receiver fixed cost' and 'Receiver reference cost' were identified to have substantial impacts on the LCOE penalty as described in Appendix C.

4. Discussion

Single and double systems configurations appear competitive with other third-generation CSP technologies [38,45,46]. Furthermore, they meet the 60 USD/MWh$_e$ target LCOE for the DOE Gen 3 programme.

In comparison with recent literature, the results from the numbering-up approach appear on the lower side. This disparity can be attributed to varying approaches, assumptions, and system parameters across studies. For instance, the studies detailed in [47,48], and [49] report an LCOE for high-temperature CSP plants that exceeds 120 USD/MWh$_e$. However, it should be noted that the CSP systems explored in these studies incorporate distinct, non-optimised configurations, with cost assumptions higher than the Gen3 targets, thereby leading to different performance and cost metrics.

As a specific example, Manzolini et al. [47] reported an LCOE of 140 USD/MWh$_e$ for a 37 MW$_e$ CSP plant utilising liquid sodium as the HTF. Their field and power block costs, however, were 1.6 to 2 times higher than the Gen3 targets. They did not take into consideration a numbered-up approach, which could yield cost reductions through multiple unit deployment. Furthermore, their assumed capacity factor is 40%, due to a lower storage capacity of 8 h.

The comparison between the systems designed demonstrates that the single large-scale 100 MW$_e$ case leads to lower LCOE than numbered-up small-scale modules. However, lower LCOE may not always lead to the highest plant revenue. The optimum configuration will be influenced by local factors, such as the availability and type of other electricity generators affecting the value of off-peak electricity prices, and the perceived risk profile, which is likely to influence the cost of financing [50].

Small-scale systems are expected to ultimately achieve higher annual energy yield due to higher efficiency heliostat fields, but results here showed that capital expenditure is a key parameter driving numbered-up systems design selection, especially for the smaller 25 and 33 MW$_e$ modules. The optimised configurations presented in this paper were obtained based on parametric analyses using discrete parameter ranges, not a global optimisation method. As a consequence, more favourable designs might have been missed in the parameter range considered. In addition, heliostat fields and receivers were designed to meet the required receiver thermal input at design point conditions without detailed consideration of annual performance, which caused a relatively small field design that hindered the capacity factor. This last point is expected to have a strong influence on LCOE. Future research should compare optimised designs based on annual performance, including field oversizing with respect to the design thermal power to compensate for seasonal DNI variations.

Numbered-up, identical systems could provide interesting opportunities for receiver and tower design manufacturing, transport and installation that could lead to significant cost reductions. Numbered-up systems could in addition provide benefits to plant operations through standardised O&M processes and natural protection against loss of revenue caused by system outages. Further research in these aspects is needed to be able to include them in the design of numbered-up CSP plants.

However, it is important to note that certain assumptions about component costs underpin these findings. As shown in the sensitivity analysis from Section 3.4, certain costs parameters, including the tower cost scaling exponent, power block reference unit price, and receiver fixed cost, significantly influence the relative LCOE difference between the optimised 2 × 50 MW$_e$ and 1 × 100 MW$_e$ configurations.

Inherent variability and uncertainty in these costs and potential future changes due to technological advances or market shifts could alter the optimal configuration. Thus, while the analysis in this study offers valuable insights for optimising solar plant configurations, the specific conclusions should be contextualised within these potential cost variations.

In this study, the solar subsystem cost share of the whole project is more strongly impacted by modularity than the remaining components. This finding, along with the sensitivity to the multiple units cost reduction factor, indicates that integrating modularity in the design of the receiver, tower and fields of new plants could benefit the overall economics of numbered-up systems. Although the numbering-and-scaling up for systems greater than 100 MW$_e$, or even GW, were out of the scope of this work, modular plant designs become compulsory in a future where vast GW-scale CSP parks are installed. They should lead to much more significant cost reduction potential than envisioned in this study, along with the aforementioned financing, commissioning, O&M and revenue loss protection.

Finally, there is a possibility that lower temperature sCO$_2$ cycles combined with commercial nitrate salt designs could lend themselves well to numbered-up systems, and improve the economic attractiveness of large-scale CSP; closer to commercially available technologies.

5. Conclusion

This paper evaluates a numbering-up approach for a 100 MW$_e$ CSP system operating a sCO$_2$ power block with an inlet temperature of 700 °C. Four alternative configurations were designed and evaluated for systems with one to four independent modules. A comprehensive techno-economic model is employed, in combination with detailed annual simulations, to generate LCOE estimates and analyse the potential of system numbering for next-generation high-temperature CSP systems based on liquid HTFs.

Results showed that a single large-scale 100 MW$_e$ module yields the lowest LCOE (54.88 USD/MWh$_e$) compared to the numbered-up systems. A two-module system exhibits a moderate increase of 2% in the LCOE without considering the improvement in system reliability. In contrast, three-module and four-module systems increase LCOE by 6.9% and 12.2%, respectively, on the assumption of constant power cycle efficiency. On the assumption that power cycle efficiency is degraded (i.e. size-dependent power block efficiency), further LCOE escalation with numbered-up systems is observed. However, multi-build savings could potentially reverse this cost escalation and a 13.9–19.6% saving on the two-module system would allow them to break even.

Finally, the sensitivity analysis of the LCOE penalty for the optimised 2 × 50 MW$_e$ configuration compared to the 1 × 100 MW$_e$ case showed that the probable LCOE penalty distribution is skewed slightly towards LCOE values above the nominal result of 6.71%, but absolute variations in LCOE penalty remain within a 10% range. It also provided critical insights into the cost parameters that significantly influence the LCOE penalty. Specifically, the tower, receiver and power block cost were found to have a substantial impact.

Finally, although the economy of scale favours large systems, other scenarios might benefit small scales and were out of scope in this work. For instance, the sensitivity of LCOE to the tower cost model to receiver size and weight could be analysed. Future work should analyse the effect of far smaller modules with cheaper steel latticework towers or interconnected modular solar subsystems with a single large-scale power block. Furthermore, more analysis is required in relation to the resilience and risk-management benefits of multi-tower systems (i.e. the impact of a failure of specific components on project financing, revenue and risk analysis when single or multiple modules are considered).

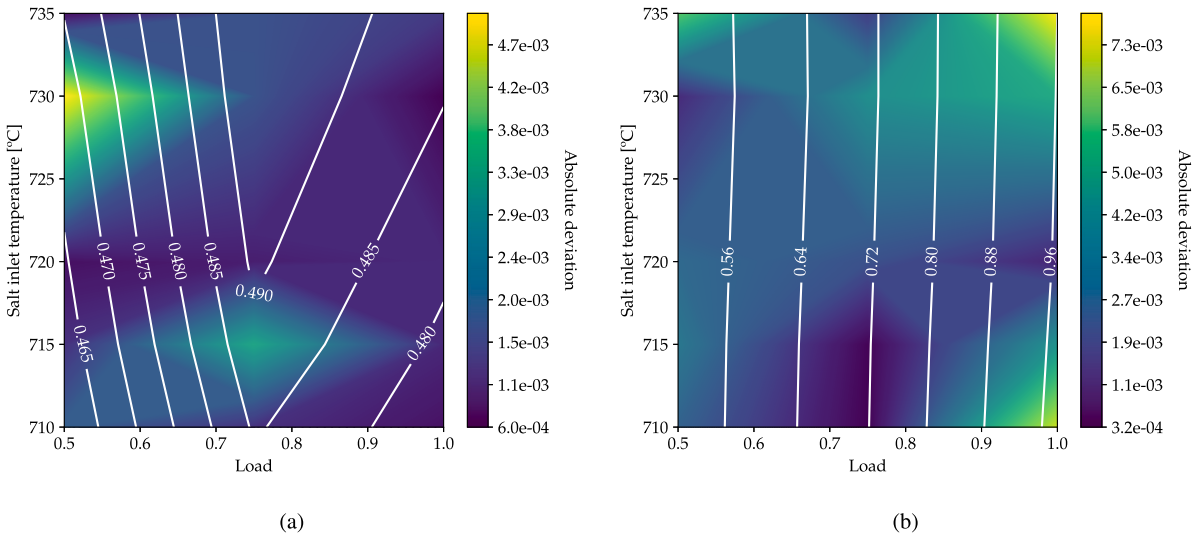

Fig. 12. Absolute deviation between the surrogate model output and the SSC off-design model output for (a) η_{PB} and (b) η_q. Ambient temperature = 20 °C. The white lines represent the values calculated using the SSC model, and the coloured bands represent the ranges of the deviations between the SSC model and the surrogate model. (For interpretation of the references to colour in this figure legend, the reader is referred to the web version of this article.)

CRediT authorship contribution statement

Charles-Alexis Asselineau: Conceptualization of this study, Methodology, Software, Writing – original draft. **Armando Fontalvo:** Conceptualization of this study, Methodology, Software, Writing – original draft. **Shuang Wang:** Methodology, Software, Writing – original draft. **Felix Venn:** Methodology. **John Pye:** Methodology, Writing – original draft. **Joe Coventry:** Conceptualization of this study, Methodology, Writing – original draft.

Declaration of competing interest

The authors declare that they have no known competing financial interests or personal relationships that could have appeared to influence the work reported in this paper.

Acknowledgements

This research was performed as part of the Australian Solar Thermal Research Institute (ASTRI), a project supported by the Australian Government, through the Australian Renewable Energy Agency (ARENA).

Appendix A. Power block surrogate model

A.1. Power block sizing

The power block sizing is conducted by executing the power block design module embedded in the SAM Simulation Core (SSC) [35]. The SSC model sizes the power block components, i.e. turbomachinery and heat exchangers, by adjusting the pressure ratio at the compressor, and the recompression fraction (i.e. the mass flow rate fraction entering re-compressor) to maximise the power block thermal efficiency. Table 8 lists the parameters employed by the SSC model to design the power cycle. More details of the on-design model can be consulted in [35] and the SAM open source code.[2]

During the on-design calculations, the power block gross output ($\dot{W}_{gross,des}$) is calculated from the power block capacity (i.e. $\dot{W}_{net}$ = 25, 33, 50 or 100 MW_e), assuming a 1% parasitic loss ($\eta_{sys,par}$ = 99%), as:

$$\dot{W}_{gross,des} = \frac{\dot{W}_{net}}{\eta_{sys,par}} \tag{31}$$

[2] https://github.com/NREL/ssc.

Table 8
Power cycle design inputs.

Parameter	Units	Value
Salt inlet temperature	°C	720
Salt outlet temperature	°C	500
CO_2 temperature at turbine inlet	°C	700
Ambient temperature	°C	35
Compressor inlet temperature	°C	41
Elevation of Daggett, CA	m	588
Compressors isentropic efficiency	–	0.87
Turbine isentropic efficiency	–	0.93
Compressor outlet pressure	MPa	25
Air cooler fan power[a]	%	2.0
LTR low pressure side pressure drop[b]	%	3.11
LTR high pressure side pressure drop[b]	%	0.56
HTR low pressure side pressure drop[b]	%	3.11
HTR high pressure side pressure drop[b]	%	0.56
PHX CO_2 side pressure drop[b]	%	0.56

[a]% of gross power.
[b]% of inlet pressure.

while ensuring that the design power of the turbine ($\dot{W}_{turb,des}$), the compressor ($\dot{W}_{comp,des}$) and the recompressor ($\dot{W}_{recomp,des}$) satisfy the relationship in Eq. (32).

$$\dot{W}_{gross,des} = \dot{W}_{turb,des} - \dot{W}_{comp,des} - \dot{W}_{recomp,des} \tag{32}$$

Within the SCC model, the design-point thermal efficiency ($\eta_{PB,des}$) is defined as in Eq. (33):

$$\eta_{PB,des} = \frac{\dot{W}_{gross,des}}{\dot{Q}_{PHX,des}} \tag{33}$$

where $\dot{Q}_{PHX,des}$ is the primary heat exchanger (PHX) thermal rating.

A.2. Off-design performance

After the design-point sizing step, detailed off-design simulations are carried out for a subset of the off-design cycle load, the salt temperature at the PHX inlet, and the ambient temperature. The cycle load is used instead of the PHX salt mass flow rate for convenience and is defined as:

$$\zeta_{PB,off} = \frac{\dot{m}_{salt,PHX}}{\dot{m}_{salt,PHX,des}} \tag{34}$$

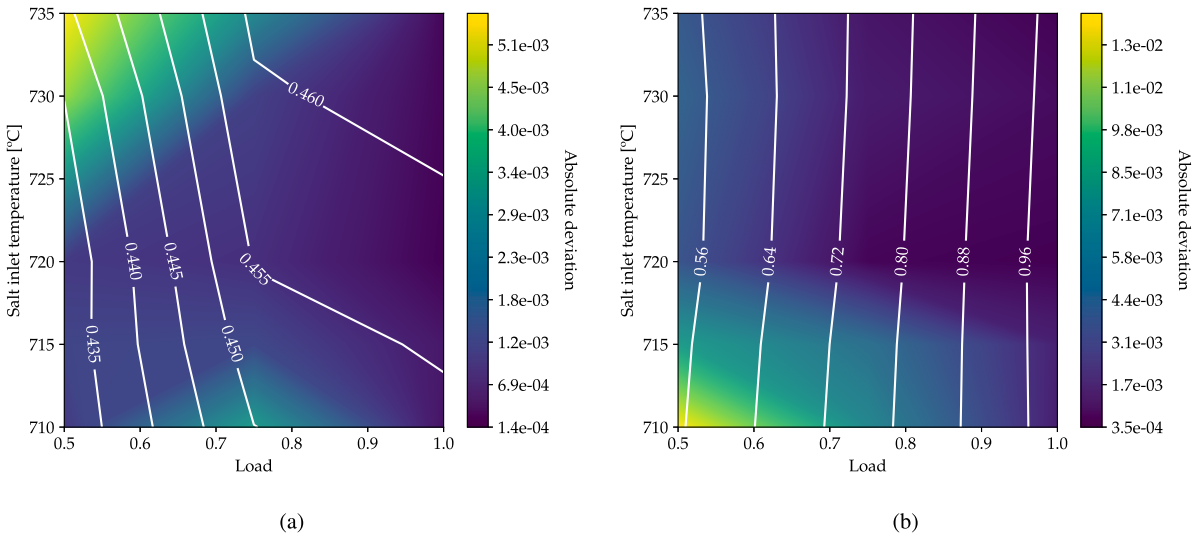

Fig. 13. Absolute deviation between the surrogate model output and the SSC off-design model output for (a) η_{PB} and (b) η_q. Ambient temperature = 40 °C. The white lines represent the values calculated using the SSC model, and the coloured bands represent the ranges of the deviations between the SSC model and the surrogate model. (For interpretation of the references to colour in this figure legend, the reader is referred to the web version of this article.)

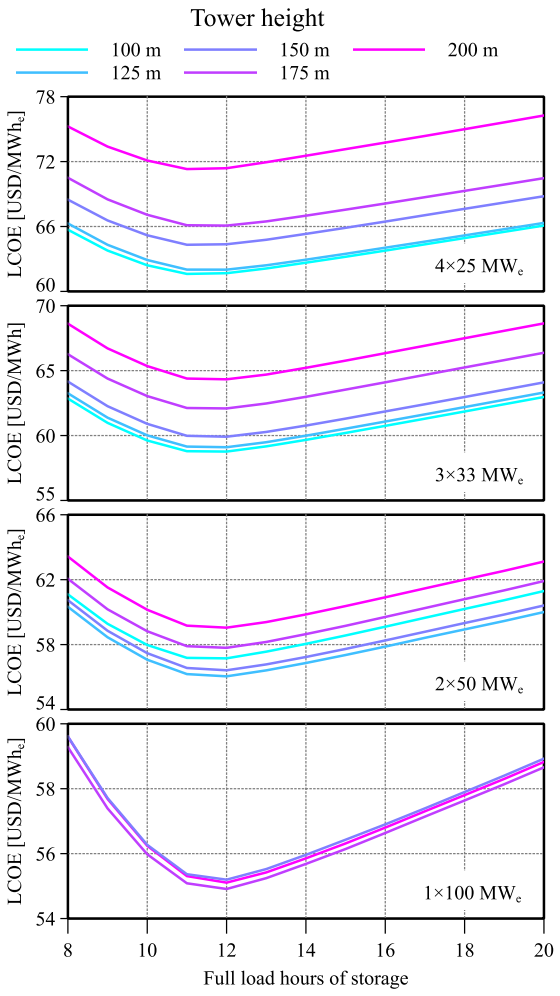

Fig. 14. Effect of full-load hours of storage and tower height on the LCOE for 100 MW_e numbered-up systems with 51% fixed power cycle efficiency. (For interpretation of the references to colour in this figure legend, the reader is referred to the web version of this article.)

where $\dot{m}_{salt,des}$ is the design salt mass flow rate, and $\dot{m}_{salt,off}$ is the off-design salt mass flow rate.

The off-design calculations are conducted by running the detailed SSC off-design model from [35]. The model estimates the power block output and thermal input for each combination of flow rate, salt temperature and ambient temperature. This is done by an internal optimisation sub-routine that maximises the heat transfer to the sCO_2 and the power output by adjusting the off-design pressure ratio and recompression fraction (i.e. the fraction of sCO_2 mass flow that goes to the re-compressor) while maintaining a constant salt temperature at the PHX outlet [35].

After the simulations are done, two off-design variables are created to define the off-design performance: the off-design thermal fraction (η_q) and the off-design thermal efficiency (η_{PB}). The off-design thermal fraction is defined as the ratio between the off-design and design-point thermal input:

$$\eta_q = \frac{\dot{Q}_{PHX}}{\dot{Q}_{PHX,des}} \tag{35}$$

while the thermal efficiency is the ratio between the off-design gross power output and the off-design thermal input:

$$\eta_{PB} = \frac{\dot{W}_{gross}}{\dot{Q}_{PHX}} \tag{36}$$

A.3. Surrogate model

A surrogate model was developed in SolarTherm to pre-process a fixed set of off-design conditions and then interpolate these data during the annual simulation using the Kriging method. In this way, SolarTherm calculates the salt temperature and mass flow rate at the PHX inlet and runs the surrogate model to calculate the off-design heat input and cycle thermal efficiency to obtain the gross power output and salt temperature at the outlet of the PHX.

Figs. 12 and 13 show the absolute deviation of the SolarTherm output from data obtained by running the detailed off-design model from the SAM simulation core. Deviations between the heat input and the gross power output between the Kriging method in SolarTherm and the SSC model are within 0.5%.

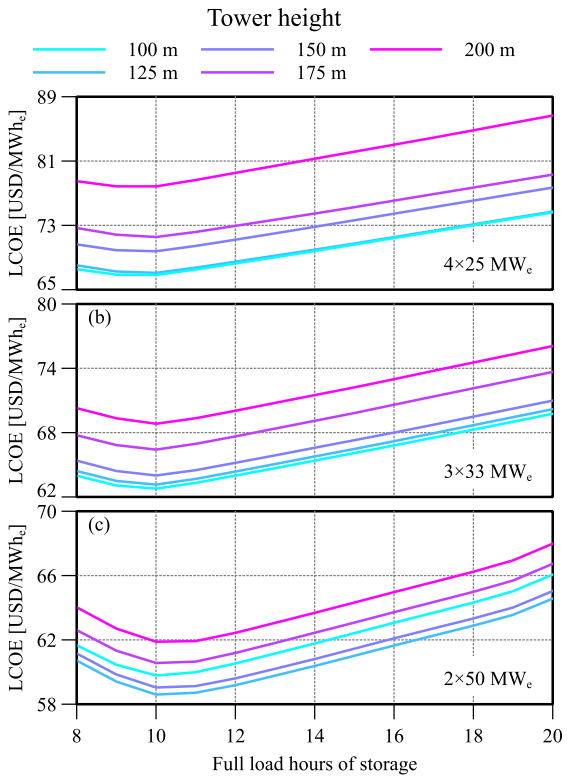

Fig. 15. Effect of full-load hours of storage and tower height on the LCOE for 100 MW$_e$ numbered-up systems with scale-dependent power cycle efficiency. (For interpretation of the references to colour in this figure legend, the reader is referred to the web version of this article.)

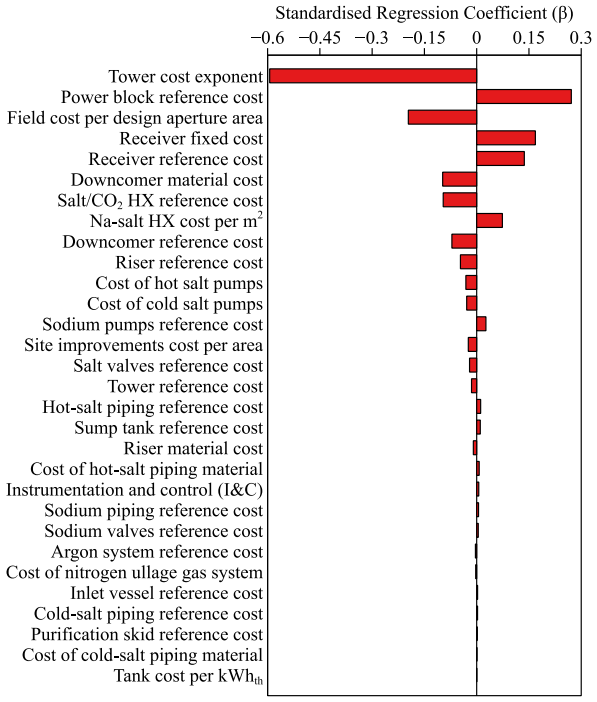

Fig. 16. Standardised regression coefficients (β) from the sensitivity analysis. Each bar corresponds to a different cost parameter in the numbered-up system configurations.

Appendix B. LCOE vs. Storage hours

This appendix presents an extension of the results presented in Sections 3.1 and 3.2. These results show the LCOE variation when sweeping the full load storage hours for each tower height. The optimal storage values reported are the ones that yield a minimum LCOE in these curves. Fig. 14 shows the LCOE obtained for all numbered configurations with a power block efficiency of 51%, while the results for the reduced rating case are shown in Fig. 15.

Appendix C. Standardised regression coefficients from sensitivity analysis

Fig. 16 presents the standardised regression coefficients (β) obtained from the sensitivity analysis discussed in Section 3.4. These coefficients represent the impact of each cost parameter on the LCOE penalty for a $2 \times 50\,\mathrm{MW_e}$ 'numbered-up' system configuration. A higher absolute value of β indicates a greater impact, with positive and negative values signifying that an increase in the corresponding parameter respectively raises or lowers the LCOE penalty.

The parameter with the greatest impact is the 'Tower cost exponent', which has a negative β value. This suggests that taller towers lead to a lower LCOE penalty, potentially making them more economical for 'numbered-up' systems. Conversely, the 'Power block reference cost' has the second most significant impact, and it is positive, indicating that higher costs in this area will lead to an increased LCOE penalty.

Similarly, parameters such as the 'Receiver fixed cost' and 'Receiver reference cost' have large positive impacts, implying that cost increases in these areas will penalise the LCOE for 'numbered-up' systems with small-scale modules. Conversely, an increase in the 'Field cost per design aperture area' parameter leads to a decrease in the LCOE penalty, as indicated by its negative β value.

Some parameters, including 'Tank cost per kWh$_{th}$' and 'Cost of cold-salt piping material', have relatively low β values, suggesting that variations in these costs have minimal impact on the LCOE penalty.

These findings demonstrate a clear relationship between individual cost components and the overall economic performance of the different system configurations, underlining the importance of careful cost management and optimisation in the design and implementation of 'numbered-up' CSP systems.

References

[1] M. Mehos, C. Turchi, J. Vidal, M. Wagner, Z. Ma, C. Ho, W. Kolb, C. Andraka, A. Kruizenga, Concentrating Solar Power Gen3 Demonstration Roadmap, Technical Report, National Renewable Energy Lab.(NREL), Golden, CO (United States), 2017, http://dx.doi.org/10.2172/1338899.

[2] A. Bonk, M. Braun, V.A. Sötz, T. Bauer, Solar Salt – Pushing an old material for energy storage to a new limit, Appl. Energy 262 (2020) 114535, http://dx.doi.org/10.1016/j.apenergy.2020.114535.

[3] J. Coventry, C. Andraka, J. Pye, M. Blanco, J. Fisher, A review of sodium receiver technologies for central receiver solar power plants, Sol. Energy 122 (2015) 749–762, http://dx.doi.org/10.1016/j.solener.2015.09.023.

[4] M. Romero, J. González-Aguilar, Next generation of liquid metal and other high-performance receiver designs for concentrating solar thermal (CST) central tower systems, in: Advances in Concentrating Solar Thermal Research and Technology, Elsevier, 2017, pp. 129–154, http://dx.doi.org/10.1016/B978-0-08-100516-3.00007-1.

[5] N. Boerema, G. Morrison, R. Taylor, G. Rosengarten, Liquid sodium versus Hitec as a heat transfer fluid in solar thermal central receiver systems, Sol. Energy 86 (9) (2012) 2293–2305, http://dx.doi.org/10.1016/j.solener.2012.05.001.

[6] C.S. Turchi, S. Gage, J. Martinek, S. Jape, K. Armijo, J. Coventry, J. Pye, C.-A. Asselineau, F. Venn, W. Logie, A. Fontalvo, S. Wang, R. McNaughton, D. Potter, T. Steinberg, G. Will, CSP Gen3: Liquid-Phase Pathway to SunShot, Technical Report, National Renewable Energy Lab.(NREL), Golden, CO (United States), 2021, http://dx.doi.org/10.2172/1807668.

[7] W.R. Logie, J.D. Pye, J. Coventry, Thermoelastic stress in concentrating solar receiver tubes: A retrospect on stress analysis methodology, and comparison of salt and sodium, Sol. Energy 160 (2018) 368–379, http://dx.doi.org/10.1016/j.solener.2017.12.003.

[8] C.J. Winter, R.L. Sizmann, L.L. Vant-Hull, Solar Power Plants: Fundamentals, Technology, Systems, Economics, Springer Berlin Heidelberg, 2012, http://dx.doi.org/10.1007/978-3-642-61245-9.

[9] P. Schramek, D.R. Mills, Multi-tower solar array, Sol. Energy 75 (3) (2003) 249–260, http://dx.doi.org/10.1016/j.solener.2003.07.004.

[10] C. Corsi, M. Blanco, J.-S. Kim, J. Pye, Point-focus multi-receiver fresnel loop – Exploring ways to increase the optical efficiency of solar tower systems, AIP Conf. Proc. 2033 (1) (2018) 170001, http://dx.doi.org/10.1063/1.5067165.

[11] P. Piroozmand, M. Boroushaki, A computational method for optimal design of the multi-tower heliostat field considering heliostats interactions, Energy 106 (2016) 240–252, http://dx.doi.org/10.1016/j.energy.2016.03.049.

[12] G. Augsburger, D. Favrat, From single-to multi-tower solar thermal power plants: investigation of the thermo-economic optimum transition size, in: Proceedings of the SolarPACES 2012 Conference on Concentrating Solar Power and Chemical Energy Systems, Vol. CONF, 2012, pp. 0–10, https://infoscience.epfl.ch/record/183589.

[13] F. Arbes, W. Landman, G. Weinrebe, M. Wöhrbach, D. Gebreiter, J.M. Estebaranz, D. Pereira, A. Jurado, Multi tower systems and simulation tools, in: AIP Conference Proceedings, Vol. 2126, AIP Publishing LLC, 2019, 030004, http://dx.doi.org/10.1063/1.5117516.

[14] Z.A. Hussaini, P. King, C. Sansom, Numerical simulation and design of multi-tower concentrated solar power fields, Sustainability 12 (6) (2020) 2402, http://dx.doi.org/10.3390/su12062402.

[15] C. Tyner, D. Wasyluk, Esolar's modular, scalable molten salt power tower reference plant design, Energy Procedia 49 (2014) 1563–1572, http://dx.doi.org/10.1016/j.egypro.2014.03.165.

[16] C. Wood, K. Drewes, Vast Solar: Improving performance and reducing cost and risk using high temperature modular arrays and sodium heat transfer fluid, in: Proceedings of the SolarPaces Conference, 2019, pp. 1–4, URL: https://api.semanticscholar.org/CorpusID:211268040.

[17] T. Neises, C. Turchi, Supercritical carbon dioxide power cycle design and configuration optimization to minimize levelized cost of energy of molten salt power towers operating at 650 °c, Sol. Energy 181 (2019) http://dx.doi.org/10.1016/j.solener.2019.01.078.

[18] DOE, SunShot Vision Study: February 2012, Technical Report, Office of Energy Efficiency and Renewable Energy, United States Department of Energy., 2012, http://dx.doi.org/10.2172/1039075, URL: https://www.osti.gov/biblio/1039075.

[19] DOE, Gen 3 CSP Topic 1 - Phase 3 Test Facility Down-Selection Criteria, Technical Report, Office of Energy Efficiency and Renewable Energy, United States Department of Energy., 2019.

[20] G. Mohan, M. Venkataraman, J. Gomez-Vidal, J. Coventry, Assessment of a novel ternary eutectic chloride salt for next generation high-temperature sensible heat storage, Energy Convers. Manage. 167 (2018) 156–164, http://dx.doi.org/10.1016/j.enconman.2018.04.100, URL: https://www.sciencedirect.com/science/article/pii/S0196890418304485.

[21] M.J. Wagner, T. Wendelin, SolarPILOT: A power tower solar field layout and characterization tool, Sol. Energy 171 (2018) http://dx.doi.org/10.1016/j.solener.2018.06.063.

[22] T. Keck, V. Schönfelder, B. Zwingmann, F. Gross, M. Balz, F. Siros, G. Flamant, High-performance stellio heliostat for high temperature application, in: AIP Conference Proceedings, Vol. 2445, AIP Publishing LLC, 2022, 120014, http://dx.doi.org/10.1063/5.0086592.

[23] Y. Wang, D. Potter, C.-A. Asselineau, C. Corsi, M. Wagner, C. Caliot, B. Piaud, M. Blanco, J.S. Kim, J. Pye, Verification of optical modelling of sunshape and surface slope error for concentrating solar power systems, Sol. Energy 195 (2020) 461–474, http://dx.doi.org/10.1016/j.solener.2019.11.035.

[24] C.-A. Asselineau, J. Pye, J. Coventry, Exploring efficiency limits for molten-salt and sodium external cylindrical receivers for third-generation concentrating solar power, Sol. Energy 240 (2022) 354–375, http://dx.doi.org/10.1016/j.solener.2022.05.001.

[25] O.J. Foust, Sodium-NaK Engineering Handbook, Gordon and Breach, New York, 1972, URL: https://www.osti.gov/biblio/4631555.

[26] S. Wang, C.-A. Asselineau, W.R. Logie, J. Pye, J. Coventry, MDBA: An accurate and efficient method for aiming heliostats, Sol. Energy 225 (2021) 694–707, http://dx.doi.org/10.1016/j.solener.2021.07.059.

[27] P. Scott, A.d.l.C. Alonso, J.T. Hinkley, J. Pye, SolarTherm: A flexible modelica-based simulator for CSP systems, AIP Conf. Proc. 1850 (1) (2017) 160026, http://dx.doi.org/10.1063/1.4984560.

[28] P. Ineichen, R. Perez, A new airmass independent formulation for the linke turbidity coefficient, Sol. Energy 73 (3) (2002) 151–157, http://dx.doi.org/10.1016/S0038-092X(02)00045-2.

[29] W.F. Holmgren, C.W. Hansen, M.A. Mikofski, Pvlib python: a python package for modeling solar energy systems, J. Open Source Softw. 3 (29) (2018) 884, http://dx.doi.org/10.21105/joss.00884.

[30] S. Wang, Design and Optimisation of a Heliostat Field and a Sodium Receiver for Next-Generation CSP Plants (Ph.D. thesis), The Australian National University, 2022, http://dx.doi.org/10.25911/P4DN-Z981.

[31] S. Wang, C.-A. Asselineau, A. Fontalvo, Y. Wang, W. Logie, J. Pye, J. Coventry, Co-optimisation of the heliostat field and receiver for concentrated solar power plants, Appl. Energy 348 (2023) 121513, http://dx.doi.org/10.1016/j.apenergy.2023.121513.

[32] M. Blanco-Muriel, D.C. Alarcón-Padilla, T. López-Moratalla, M. Lara-Coira, Computing the solar vector, Sol. Energy 70 (5) (2001) 431–441, http://dx.doi.org/10.1016/S0038-092X(00)00156-0.

[33] H. Akima, A new method of interpolation and smooth curve fitting based on local procedures, J. ACM 17 (4) (1970) 589–602, http://dx.doi.org/10.1145/321607.321609.

[34] S. Guccione, A. Fontalvo, R. Guedez, J. Pye, L. Savoldi, R. Zanino, Techno-economic optimisation of a sodium–chloride salt heat exchanger for concentrating solar power applications, Sol. Energy 239 (2022) 252–267, http://dx.doi.org/10.1016/j.solener.2022.04.052.

[35] T. Neises, C. Turchi, Supercritical carbon dioxide power cycle design and configuration optimization to minimize levelized cost of energy of molten salt power towers operating at 650° c, Sol. Energy 181 (2019) 27–36, http://dx.doi.org/10.1016/j.solener.2019.01.078.

[36] NREL, System advisor model version 2020.11.29 (SAM 2020.11.29), 2020, URL: https://sam.nrel.gov/download/version-2021-12-01.html.

[37] N. Blair, A. Dobos, J. Freeman, T. Neises, M. Wagner, T. Ferguson, P. Gilman, S. Janzou, System Advisor Model, SAM 2014.1.14: General Description, NREL/TP-6A20-6101, NREL, National Renewable Energy Laboratory, Golden, CO., 2014, http://dx.doi.org/10.2172/1126294.

[38] A. Fontalvo, S. Guccione, Y. Wang, S. Wang, Z. Kee, C.-A. Asselineau, D. Potter, F. Venn, J. Martinek, C. Turchi, et al., System-level comparison of sodium and salt systems in support of the Gen3 liquids pathway, in: AIP Conference Proceedings, Vol. 2445, AIP Publishing LLC, 2022, 030007, http://dx.doi.org/10.1063/5.0087911.

[39] B.D. Kelly, Advanced Thermal Storage for Central Receivers with Supercritical Coolants, Technical Report, Abengoa Solar Inc., 2010, http://dx.doi.org/10.2172/981926.

[40] D. Wait, Development of 800°C Integrated Flow Channel Ceramic Receiver, Technical Report, SolarReserve LLC, 2018, http://dx.doi.org/10.2172/1460529, URL: https://www.osti.gov/biblio/1460529.

[41] A. Farinelle, Conception and Design of a Solar Receiver Working with Sodium as Heat Transfer Fluid (Master's thesis), Universidad de Zaragoza, 2016, p. 41.

[42] DOE, Generation 3 concentrating solar power systems, funding opportunity announcement (FOA) number: DE-FOA-0001697, 2017, URL: https://www.energy.gov/eere/solar/funding-opportunity-announcement-generation-3-concentrating-solar-power-systems-gen3csp.

[43] L.P. Swiler, G.D. Wyss, A User's Guide to Sandia's Latin Hypercube Sampling Software: LHS UNIX Library/standalone Version., Technical Report, Sandia National Laboratories (SNL), Albuquerque, NM, and Livermore, CA ..., 2004, http://dx.doi.org/10.2172/919175.

[44] B.M. Adams, W.J. Bohnhoff, K.R. Dalbey, M.S. Ebeida, J.P. Eddy, M.S. Eldred, R.W. Hooper, P.D. Hough, K.T. Hu, J.D. Jakeman, et al., Dakota, a Multilevel Parallel Object-Oriented Framework for Design Optimization, Parameter Estimation, Uncertainty Quantification, and Sensitivity Analysis: Version 6.13 User's Manual, Technical Report, Sandia National Lab.(SNL-NM), Albuquerque, NM (United States), 2020, http://dx.doi.org/10.2172/1817318.

[45] L.F. González-Portillo, K.J. Albrecht, J. Sment, B. Mills, C.K. Ho, Sensitivity analysis of the levelized cost of electricity for a particle-based CSP system, in: Energy Sustainability, Vol. 84881, American Society of Mechanical Engineers, 2021, V001T02A008, http://dx.doi.org/10.1115/ES2021-63223.

[46] L.F. González-Portillo, K. Albrecht, C.K. Ho, Techno-economic optimization of CSP plants with free-falling particle receivers, Entropy 23 (1) (2021) 76, http://dx.doi.org/10.3390/e23010076.

[47] G. Manzolini, M. Binotti, D. Bonalumi, C. Invernizzi, P. Iora, CO2 mixtures as innovative working fluid in power cycles applied to solar plants. Techno-economic assessment, Sol. Energy 181 (2019) 530–544, http://dx.doi.org/10.1016/j.solener.2019.01.015.

[48] C.S. Turchi, J. Vidal, M. Bauer, Molten salt power towers operating at 600–650 C: Salt selection and cost benefits, Sol. Energy 164 (2018) 38–46, http://dx.doi.org/10.1016/j.solener.2018.01.063.

[49] M.A. Meybodi, A. Beath, S. Gwynn-Jones, A. Veeraragavan, H. Gurgenci, K. Hooman, Techno-economic analysis of supercritical carbon dioxide power blocks, in: AIP Conference Proceedings, Vol. 1850, AIP Publishing, 2017, http://dx.doi.org/10.1063/1.4984409.

[50] M.A. Meybodi, A.C. Beath, Impact of cost uncertainties and solar data variations on the economics of central receiver solar power plants: An Australian case study, Renew. Energy 93 (2016) 510–524, http://dx.doi.org/10.1016/j.renene.2016.03.016.